The Pennsylvania State University
The Graduate School

HYBRID APPROACH FOR MANUFACTURING STIFFENED STRUCTURES USING COLD SPRAY DEPOSITION

A Thesis in
Engineering Science and Mechanics
by
Michael Hennessey

Submitted in Partial Fulfillment
of the Requirements
for the Degree of

Master of Science

December 2023

The thesis of Michael Hennessey was reviewed and approved by the following:

Matthew H. Lear
Assistant Research Professor, Engineering Science and Mechanics
Thesis Adviser

Timothy J. Eden
Research Professor, Engineering Science and Mechanics

Jeremy M. Schreiber
Associate Research Professor, Engineering Science and Mechanics

Albert Segall
Professor, Engineering Science and Mechanics
Head of the Engineering Science and Mechanics Graduate Program

Abstract

Recent advancements in the consistency and reliability of cold spray (CS) technology have increased interest in using cold spray as an additive manufacturing (AM) method. The challenge in employing this technology, similar to any additive manufacturing method, is the ability to guarantee isotropic mechanical properties of the AM part that are comparable to wrought material. The goal of this research effort is to prove parts made with a hybrid approach using 6061 powder and 6061-T6 wrought aluminum substrate performs comparably to a part machined entirely from wrought aluminum (6061-T6). CS parameters were verified through adhesion testing, interfacial imaging, coating pass thickness measurements, and tensile testing of 100% cold sprayed dogbone specimens. T-channel specimens were manufactured using CS deposition, representing a plate with a rib to stiffen the structure. Two types of T-channels, CS coating and wrought aluminum, were tested in four-point bending. Strain, force, and displacement data were collected. Specimens were sectioned and imaged with optical microscopy and scanning electron microscopy, before and after testing to study the effect of a bending load on coating quality. A finite element model was built to compare with empirical data collected from four-point bend testing. Johnson-Cook plasticity was used to model the plastic behavior of the cold sprayed parts. Johnson-Cook parameters were tuned using tensile test data for the 6061 powder. Tensile data and four-point bending results indicated that cold sprayed specimens had strength and stiffness comparable to the wrought specimens with an expected reduction in ductility that is inherent in cold sprayed coatings. Future work should look to apply the hybrid approach for different geometries and investigate the effects of fatigue loading on the coating interface.

Table of Contents

List of Figures

List of Tables

Acknowledgments

I would like to thank Tony Naccarelli, Matt Wagner, Chris Wertz, John Potter, Cody Wassel, and Julie Anderson for helping me complete my research. Special thanks to Dr. Matt Lear, Dr. Jeremy Schreiber and Dr. Tim Eden for being my committee members and for their guidance in not only completing my graduate degree, but making it a rewarding experience.

Chapter 1 Introduction

The first patent for cold spray (CS) was filed in the United States on March 23, 1900 by Samuel Thurston. Thurston's technology used pressurize gas to embed metallic particles in metal plates to form a coating. Thurston's system achieved 350 m/s particle velocities at room temperature, limiting the possible material options. Cold spray was then rediscovered in the late 1980s by Russian scientists during wind tunnel tests on two-phase flow . It was observed that at certain supersonic velocities, the fine powder would begin to buildup on the test article, rather than erode. Anatoli Papyrin and his colleagues at the Institute of Theoretical and Applied Mechanics of the Siberian Division fo the Russian Academy of Science (ITAM SB RAS) in Novosibirsk observed the deposition of metallic particles at supersonic speeds onto a substrate [1]. Unlike Thurston's efforts, deposition was successful for a wide range of materials - metals, alloys, polymers, and composites. Papyrin moved to the US in the 1990s bringing cold spray technology along with him. He founded a cold spray system at the National Center for Manufacturing Sciences (NCMS) resulting in a US patent filing in 1994 for cold spray technology [1]. Dr. Papyrin went on to the Pennsylvania State University (PSU) where the system was redesigned. Cold spray research is ongoing at PSU and cold spray technology continues to grow globally.

In the CS process, a high pressure process gas - typically nitrogen (N_2) or helium (He) - is heated and expanded to supersonic speeds using a DeLaval (converging-diverging) nozzle. Solid powder particles are injected in the gas stream as it enters the nozzle. The expanding gas accelerates the particles to speeds ranging from 300 to 1000 m/s.

The high velocity particles impact a substrate and undergo plastic deformation. When the particles exceed a critical velocity, they form strong mechanical bonds between the substrate and previously deposited particles. Figure 1.1 shows an overview of the cold spray process. Cold spray offers several advantages compared to other thermal processes:

- Minimal heat input to substrate,
- Minimal oxide content in the deposition,
- No phase changes,
- Higher bond strength,
- Compressive residual stress,
- High strength, and
- High hardness.

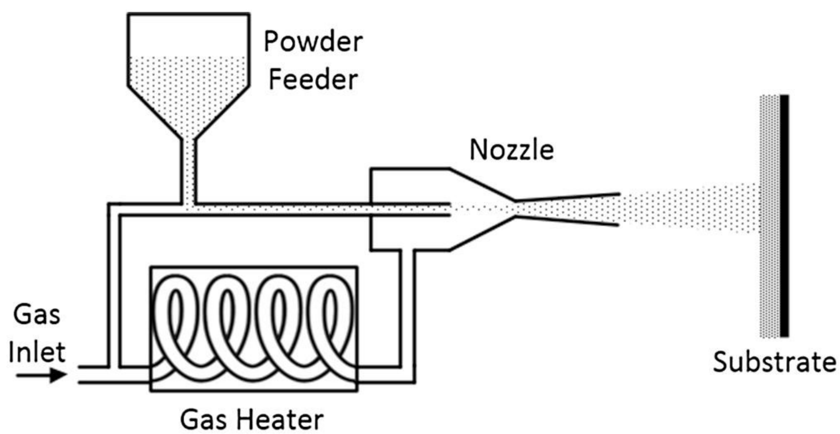

Figure 1.1. Overview of Cold Spray Deposition Process [2]

The aim of this research is to demonstrate a hybrid approach to manufacturing aluminum 6061 components that leverages the advantages of cold spray (additive manufacturing) and traditional machining (subtractive manufacturing). Cold spray's strengths as an additive manufacturing approach are high deposition rates, minimal heat affected zone, and excellent material properties when utilizing helium as the main process gas. Traditional machining excels at high precision parts using a well-defined process and reduced need for quality control compared to additive manufacturing methods. Traditional machining's main deficits are material waste and processing time to achieve the net shape. Depending on complexity of the geometry, material waste can be as high as 90% [3]. Cold spray and traditional subtractive manufacturing, in combination, could limit the amount of material waste and reduce the amount of machining time required to produce final part geometry.

In this paper, the cold spray process is developed for deposition of 6061 powder onto a 6061-T6 substrate. The powder was characterized by performing the particle size distribution (PSD) analysis, completing optical and scanning electron microscopy, and performing tensile testing of CS dogbone specimens composed of 100% cold spray powder. Key process parameters for producing a quality coating were gas pressure, gas temperature, powder feed rate, nozzle stand-off, and traverse rate. The resultant coating was verified for quality through adhesion testing in accordance with ASTM D4541, coating thickness measurements for deposition rate verification, and optical microscopy of the interface taken from a spare specimen. With the optimized cold spray process parameters, specimens were produced and tested in four-point bending for direct comparison with machined wrought aluminum specimens. A finite element analysis (FEA) was completed and compared with empirical data.

Chapter 2
Literature Review

2.1 Introduction

This chapter covers the cold spray process, cold spray additive manufacturing (CSAM), and background of the Johnson-Cook plasticity model used for the finite element analysis (FEA).

2.2 Cold Spray Deposition

Cold spray deposition contains a plethora of process parameters that contribute to mechanical properties and deposition efficacy. Early research in cold spray revealed a critical velocity (V_{cr}) threshold where solid particles began to bond to the substrate rather than bounce away. The critical velocity is calculated based on several process parameters and the material properties of the particles being deposited. An empirical relationship (Eq. 2.1), was developed by Assadi et al. to characterize the critical velocity [4]. The equation accounts for the following particle properties: density (ρ), melt temperature (T_m), ultimate strength (σ_u), and temperature at nozzle exit (T_i). Carrier gas parameters which influence critical velocity are pressure, temperature, and density. Particle-related parameters are particle size, morphology, mechanical properties, thermal properties, and density [5]. Increases to gas pressure and temperature result in increased deposition efficiencies (DE). Deposition efficiency is defined as the mass of powder deposited divided by the mass of powder that impacted the substrate. Figure 2.1 displays the impact of pressure and temperature on DE [6]. Temperature has a larger effect than pressure with a 40% increase across the tested temperature range compared to a 20% increase of the tested pressure range. The larger gains in DE are likely due to thermal softening effects and increased plastic deformation of the particles upon impact. Deposition efficiency is important when calculating the cost to apply a CS coating - discussed later in Section 2.4.

$$v_{crit} = 667 - 14\rho + 0.08T_m + 0.1\sigma_u - 0.4T_i \tag{2.1}$$

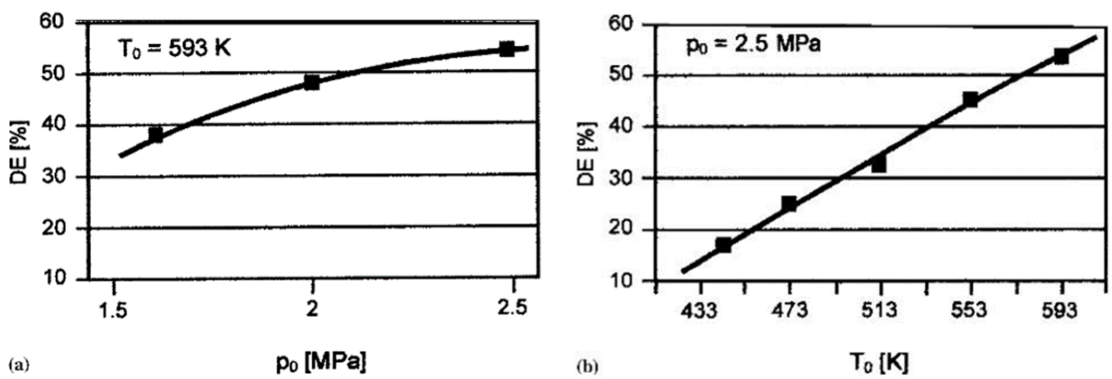

Figure 2.1. Pressure and temperature effects on cold spray deposition efficiency [6]

2.2.1 Cold Spray Powders

Powders have a significant impact on the effectiveness of cold spray deposition. The powders must be sufficiently ductile to plastically deform upon impact with the substrate, fall within a range of particle size and shape, and be able to flow through the feeder as seen in Figure 1.1. Hardness and ductility influence the particle's deformation characteristics. All of these parameters are affected by the production method used to create the powder. Powders are sometimes annealed during the pre-processing stage to remove internal stresses, improve ductility, and decrease hardness. To control particle size, powders are often sieved to remove particles below a certain diameter from the powder batch. A narrower distribution in particle sizes results in better powder flow and higher deposition rates. Particle Size Distribution analyses (PSD) are completed to characterize the range of particle sizes that can be expected for a given powder. PSD results vary based on powder type, manufacturing method, and manufacturer, but they provide insight into the process parameters required to optimize deposition. Figure 2.4 is an example of a PSD completed for an aluminum powder. The importance of a powder's PSD stems from the effect of particle diameter on velocity and temperature.

Particles of different sizes have different velocities and temperatures when injected through the same cold spray system [7]. Particle size affects the critical velocity. Helfritch and Champagne built upon the critical velocity equation (Eq.2.1) and implemented a deposition efficiency based upon particle size [8]. Particles in cold spray powders are not uniform but have a distribution of particle diameters. Particles that are below a minimum diameter (dependent on particle density) are adversely affected by the shockwave created just after nozzle exit. Figure 2.2 illustrates the location of the shockwave relative to nozzle exit during deposition of a 3μm copper particle. Gas velocity drops significantly across the shock. Small diameter particles - on the order of 2μm or less - are extremely dependent on gas velocity to maintain their momentum. Figure 2.3 shows that there is a bounded region for particle diameters to achieve a critical velocity. Particles that are too large require too much energy to accelerate to the critical velocity. Small particles that are affected by the shockwave impact the substrate below the critical velocity and do not bond. Equation 2.2 is the resulting formula for calculating the deposition efficiency based upon particle size. Particles smaller than the smallest diameter achieving critical velocity are subtracted from the percentage of particles smaller than the largest particle achieving critical velocity. This removes the particle diameters on either end of the distribution that are either too large to achieve critical velocity, or too small to be unaffected by the downstream shockwave [8].

$$DE = \frac{100}{2} * (1 + erf(\frac{d_p - MMD}{\sigma/\sqrt{2}})) \tag{2.2}$$

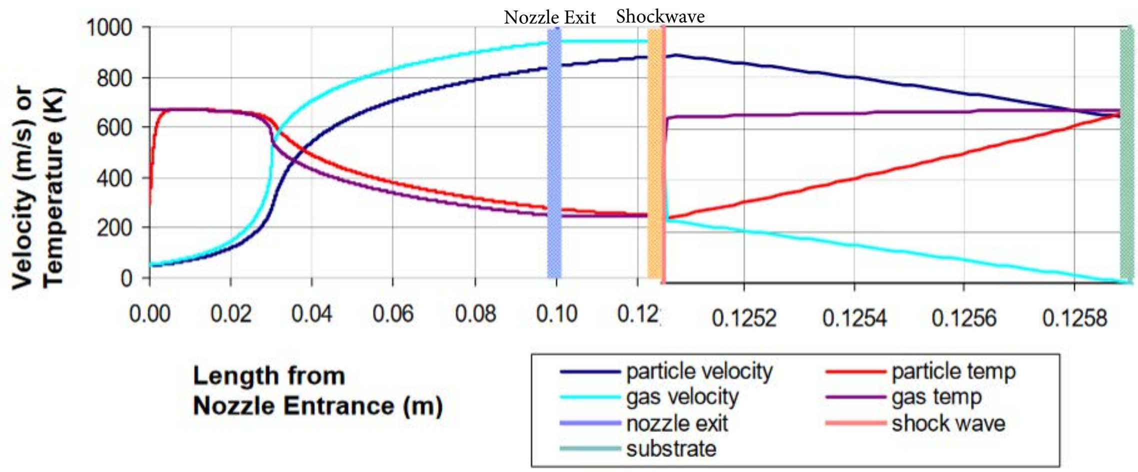

Figure 2.2. Particle velocity and temperature as it travels through a nozzle and impacts a substrate [8].

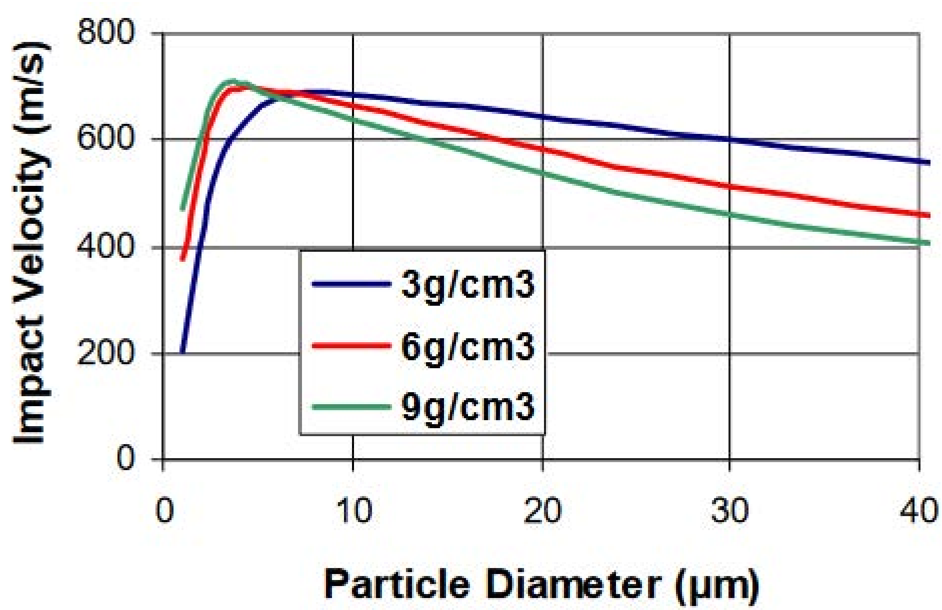

Figure 2.3. Particle velocities for various particle diameters for three particle densities. Higher density particles' impact velocities are more sensitive to particle size [8].

Result Analysis Table

ID: AluminumPraxairAl10 Run No: 13		Measured: 9/25/07 2:52PM
File: NOV33	Rec. No: 3	Analysed: 9/25/07 2:52PM
Path: C:\SIZERS\DATA\MAGDA\		Source: Analysed
Range: 300RF mm Beam: 2.40 mm Sampler: MS1		Obs': 14.2 %
Presentation: 3_AL2O3 Analysis: Polydisperse		Residual: 1.001 %
Modifications: None		
Conc. = 0.0421 %Vol	Density = 2.400 g/cm^3	S.S.A.= 0.1213 m^2/g
Distribution: Volume	D[4, 3] = 25.23 um	D[3, 2] = 20.61 um
D(v, 0.1) = 12.62 um	D(v, 0.5) = 23.46 um	D(v, 0.9) = 40.43 um
Span = 1.185E+00	Uniformity = 3.678E-01	

Size (um)	Volume In %	Size (um)	Volume In %	Size (um)	Volume In %	Size (um)	Volume In %
0.05	0.00	0.58	0.00	6.63	0.74	76.32	0.00
0.06	0.00	0.67	0.00	7.72	1.39	88.91	0.00
0.07	0.00	0.78	0.00	9.00	2.40	103.58	0.00
0.08	0.00	0.91	0.00	10.48	3.87	120.67	0.00
0.09	0.00	1.06	0.00	12.21	5.88	140.58	0.00
0.11	0.00	1.24	0.00	14.22	8.33	163.77	0.00
0.13	0.00	1.44	0.00	16.57	10.78	190.80	0.00
0.15	0.00	1.68	0.00	19.31	12.51	222.28	0.00
0.17	0.00	1.95	0.00	22.49	13.17	258.95	0.00
0.20	0.00	2.28	0.00	26.20	13.03	301.68	0.00
0.23	0.00	2.65	0.00	30.53	10.65	351.46	0.00
0.27	0.00	3.09	0.00	35.56	7.80	409.45	0.00
0.31	0.00	3.60	0.00	41.43	5.03	477.01	0.00
0.36	0.00	4.19	0.00	48.27	2.76	555.71	0.00
0.42	0.00	4.88	0.16	56.23	1.15	647.41	0.00
0.49	0.00	5.69	0.35	65.51	0.00	754.23	0.00
0.58		6.63		76.32		878.67	

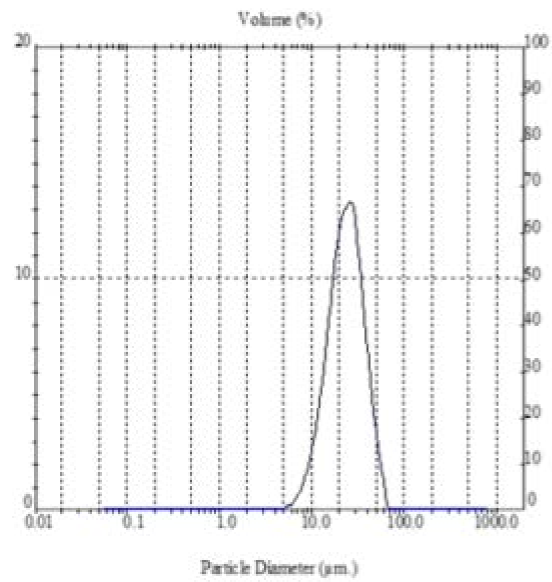

Figure 2.4. Particle Size Distribution (PSD) example for a commercially pure aluminum powder [7].

2.2.2 Process Gases

The main process gas and its properties have a significant impact on the cold spray process and the coating produced. It has been demonstrated that lower density gases, particularly helium, are more effective in depositing powder onto substrates [9]. Helium's thermal conductivity is 0.149 $\frac{W}{m°C}$ compared to inert nitrogen's 0.026$\frac{W}{m°C}$. In addition to thermal conductivity, helium's specific gas constant (R) and specific heat ratio (k) give it superior heat transfer properties relative to N_2. R and k values for helium are 2077 J/kg-K and 1.667, respectively. R and k values for N_2 are 297 J/kg-K and 1.4, respectively. Equation 2.4 is the ratio of the sonic velocity of helium and the sonic velocity of nitrogen at the same temperature. At the same Mach number, helium can achieve velocities almost 3x that of N_2. Higher particle velocities and improved heat transfer result in improved coating density, higher ductility, and increased adhesion strength [7]. The higher ductility is especially important in structural applications where parts experience high levels of strain. Loss of ductility is inherent to cold spray because of the work hardening particles experienced as they undergo plastic deformation. The comparison of spraying with N_2 and He can be seen graphically in Figures 2.5 and 2.6. The increase in impact velocity results in a larger window where deposition occurs. The distribution of particle sizes that experience deposition also widens. When using nitrogen as the process gas, only particles 2-10 μm in diameter will successfully bond to the substrate. For helium, the particle window increases to 10-50 μm with smaller particles exceeding the erosion velocity. As mentioned previously, sieving the powder can eliminate particles less than 10 μm - eliminating erosion and increasing deposition efficiency. The benefits of helium are unquestionable; however, the cost can be prohibitive in some applications. Helium is a finite and decreasing resource [9]. Consequently, current prices list N_2 at \$0.04 per cubic foot where helium is \$0.55 per cubic foot, more than 13 times as expensive. The financial impact can be prohibitive if the part is small or of inconsequential value - explored further in Section 2.4.

$$Mach(M) = \frac{\text{Gas Velocity}}{\text{Speed of Sound (a)}} = \frac{V_g}{\sqrt{kRT}} \tag{2.3}$$

$$\frac{a_{He}}{a_{N_2}} = \sqrt{\frac{(kRT_{He})}{(kRT_{N_2})}} = 2.9 \tag{2.4}$$

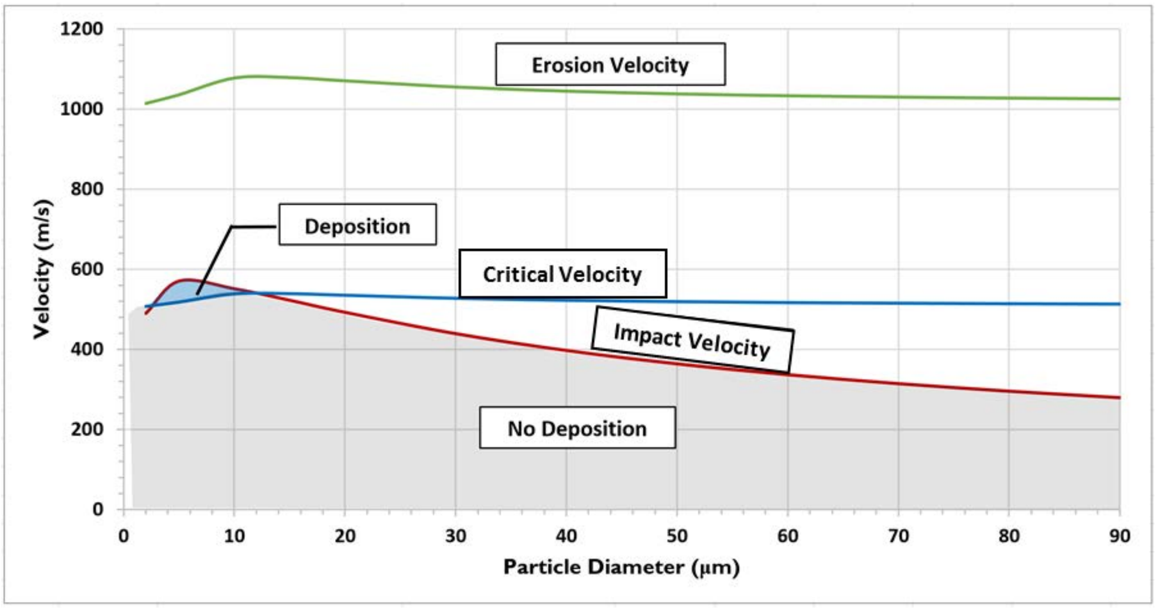

Figure 2.5. Plot of Impact, Critical and Erosion Velocity for Cu using N_2 as the main process gas at P=30 bar and T=300°C [7]

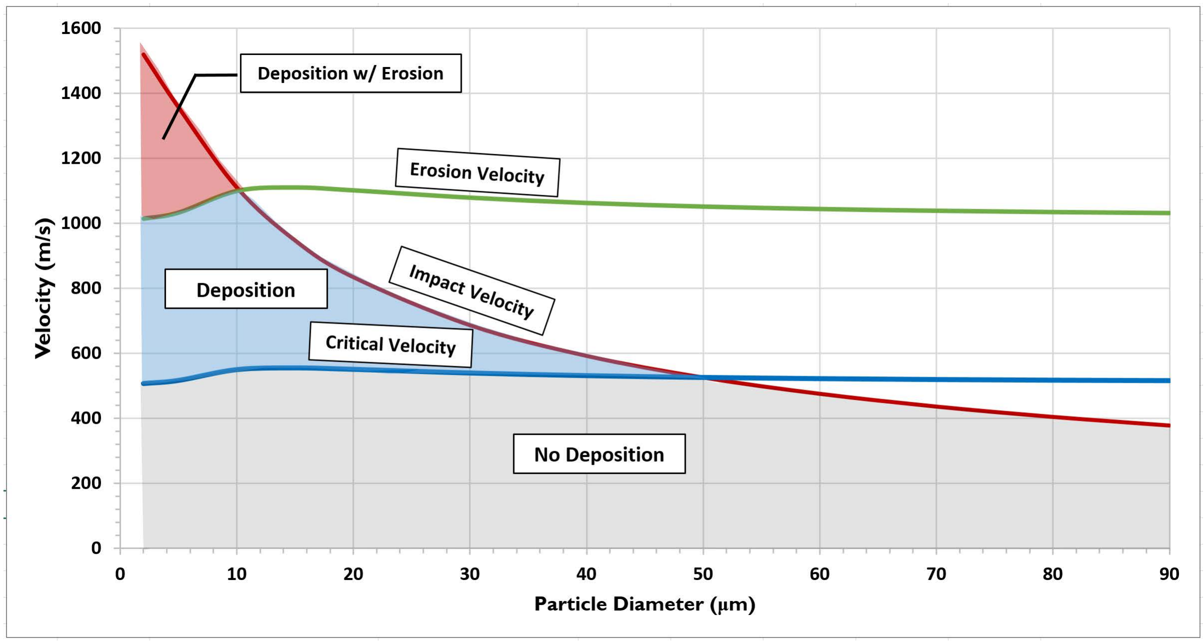

Figure 2.6. Plot of Impact, Critical and Erosion Velocity for Cu using He as the main process gas at P=30 bar and T=300°C [7]

2.2.3 Cold Spray Bonding

The fundamental mechanism of particle bonding is not fully understood. The bonding mechanism and quality of the bond is dependent upon a number of factors. Namely, the hardness of particle and substrate, impact temperature, powder material properties, oxide layer thickness of the particle, and the particle's impact velocity. The substrate is equally as important as the CS particles. A substrate with high hardness can result in CS particles bouncing off, while a substrate that is too soft results in little plastic deformation at the surface. Surface roughness and the oxide layer of the substrate affect adhesion characteristics. For aluminum on aluminum (soft particle on soft substrate), mechanical bonding and metallurgical bonding are present. Plastic deformation occurs in both particle and substrate (or previously deposited particles) resulting in a very high strength bond, with metallurgical bonding providing a higher bond strength than mechanical bonding [7]. One theory on the particle bonding mechanism is the presence of adiabatic shear instabilities. These instabilities produce localized shear at the particle-substrate interface which promote adhesion and bonding [4, 10]. Other research claims that adiabatic shear instability is not necessary for cold spray bonding. Instead, it is postulated that the large interfacial strains are a result of strong pressure waves induced by the impact velocity of the particle [5, 11]. While the bonding mechanism research is ongoing, current practice is to use Eq. 2.1 for critical velocity to determine the required system parameters to achieve a quality CS coating.

2.3 Cold Spray Additive Manufacturing (CSAM)

Initially used as a coating process, advancements in CS technology and improved process control have increased interest in using cold spray as an additive manufacturing process (CSAM) [12–15]. Theoretically, cold spray deposition has no thickness limitation and has one of the highest deposition rates of any additive manufacturing process making it an attractive option [16]. However, as seen in figure 2.7, feature size is directly proportional to deposition rate resulting in lower resolution features. This trade space is where a hybrid approach combining cold spray deposition and traditional machining processes could result in a part with less material waste and equal to, or better, thermal and mechanical properties than wrought material.

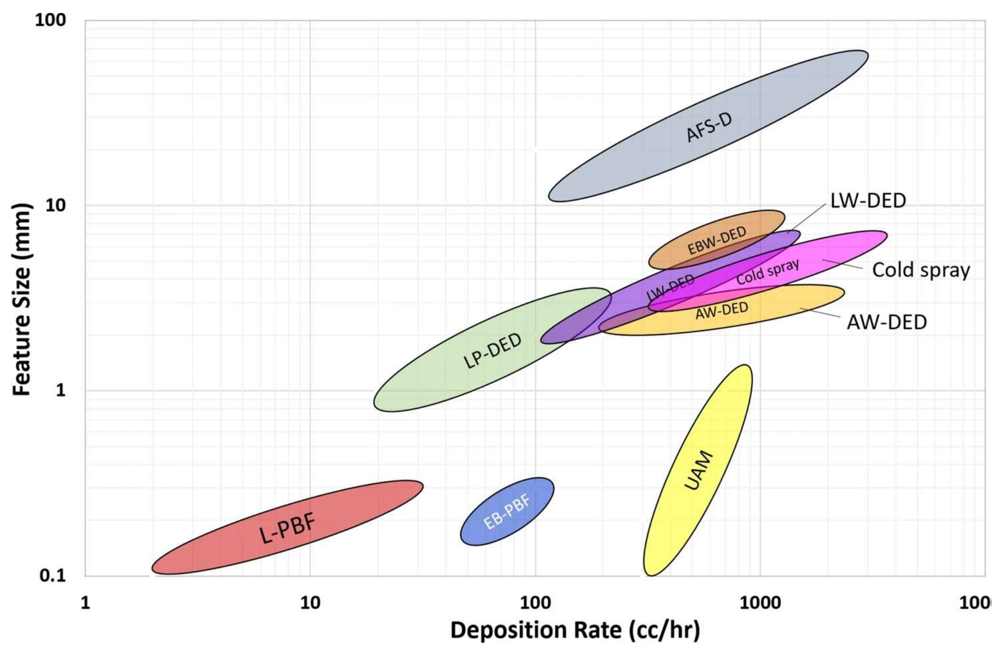

Figure 2.7. Feature Size and Deposition Rates for Various AM Processes [17].

CSAM is a subset of cold spray technology focused on creating complete parts or building onto existing structures. Two techniques are used for CSAM depending upon the size of the part being fabricated. If the part is lightweight, the CSAM process occurs similar to plastic 3D printing where the print bed moves and the nozzle is fixed. A crossover point exists where the size and weight of the part requires the nozzle to be manipulated with a robotic arm rather than the part itself. Manipulating the nozzle maintains deposition rates and eliminates the need to design robust systems capable of manipulating parts that weight hundreds of pounds. While not yet commercially commonplace, companies such as SPEE3D, Titomic, and VRC Metal Systems are all entering into the additive manufacturing domain using cold spray technology. SPEE3D (Australia) is successfully leveraging the cold spray process to create a novel additive manufacturing technology. Their metal printers can create parts out of copper or aluminum that are up to one meter in diameter with a maximum deposition rate of 100 g/min. Using compressed air at 30 bar (450 psi), their LightSPEE3D printer is capable of producing aluminum components with strengths exceeding those of cast parts after a post-process heat treatment that allows them to recover some of the ductility lost during the cold spray process. Table 2.1 displays the mechanical properties achieved by a SPEE3D metal printer for aluminum 6061. Titomic (Australia) has scaled to even larger build capabilities. Titomic's TKF 9000 system has a build volume of 40 cubic meters and a maximum deposition rate of 30 kg/hr dependent on the powder material, about 5x the capabilities of SPEE3D's offerings.

Table 2.1. SPEE3D Aluminum Material Properties [18]

	SPEE3D Printed	**Wrought**
	Al 6061 as heat treated	**6061-T6**
Yield Strength (MPa)	160 (min)	240
Ultimate Strength (MPa)	220 (min)	260
Elongation	4.5% (min)	8%
Hardness Rockwell B	36 (typical)	55

Leveraging cold spray for a hybrid approach introduces other benefits inherent to cold spray produced parts. Cold spray has demonstrated multi-material capabilities, improved fatigue performance [19,20], and improved wear resistance. Fatigue life improves for aluminum specimens due to compressive residual stresses imparted into the substrate during the coating process [2, 19, 20]. Improved wear resistance was observed by Wolfe et al. where a chromium carbide coating was deposited onto 4140 alloy steel [21]. The hybrid approach proposed, shown in Figure 2.8, leverages the high deposition rate of cold spray to add localized features onto bulk wrought material to then machine into the final form. The addition of localized features to wrought material prevents the need to build the part up from scratch and takes advantage of both processes - subtractive and additive. Bulk material can be purchased in its leanest form and cold spray can locally add features to fit the needs of the application. This process allows for different materials to be used depending on the application of the feature. Using dissimilar materials opens up an infinite number of possibilities for the hybrid approach. With an aluminum substrate, copper coatings could be deposited for heat transfer benefits, or a harder coating for improved wear resistance as mentioned previously [22].

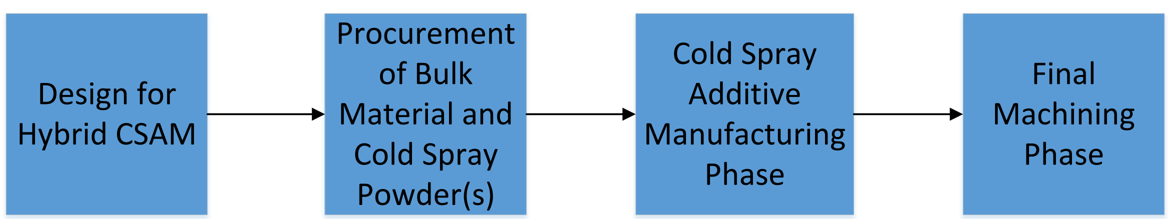

Figure 2.8. Workflow for hybrid manufacturing approach.

For structural repair and additive manufacturing using cold spray deposition, aluminum 6061 is a natural starting point. Aluminum 6061 alloy is heavily researched for cold spray due to its widespread usage in engineering applications and its favorable material properties for cold spray deposition. Cold spray also eliminates risks introduced by other non solid-state, thermal spray techniques like oxidation, porosity, and heat affected zone resulting in loss of strength. The critical velocity of aluminum 6061 is 600 m/s, dependent on particle size [23]. Single particle impacts, microstructure characterization, and machinability of 6061 coatings are all examples of characterizing aluminum 6061 in various stages of the cold spray operation [13, 24, 25]. Work has also been completed to reclaim some of the ductility lost during deposition [18,26]. Parameters for cold spraying aluminum 6061 onto aluminum 6061 are well understood for producing a uniform, low porosity coating with strengths comparable to wrought aluminum. As a result, there is high confidence in the ability to consistently produce quality coatings in the context of an additive manufacturing application for aluminum 6061 components.

2.4 Cold Spray Economics

Estimation of cold spray costs can be divided into two categories: non-recurring and recurring. Figure 2.9 provides an overview of the costs in each category. Existing facilities and equipment were used so no start-up or infrastructure costs were incurred. Non-recurring costs were ignored for this research effort. The recurring costs used to calculate the price per specimen were process gasses, cold spray powders, substrates, and electricity usage. Figure 2.10 details the information needed to estimate the cost of a cold spraying procedure.

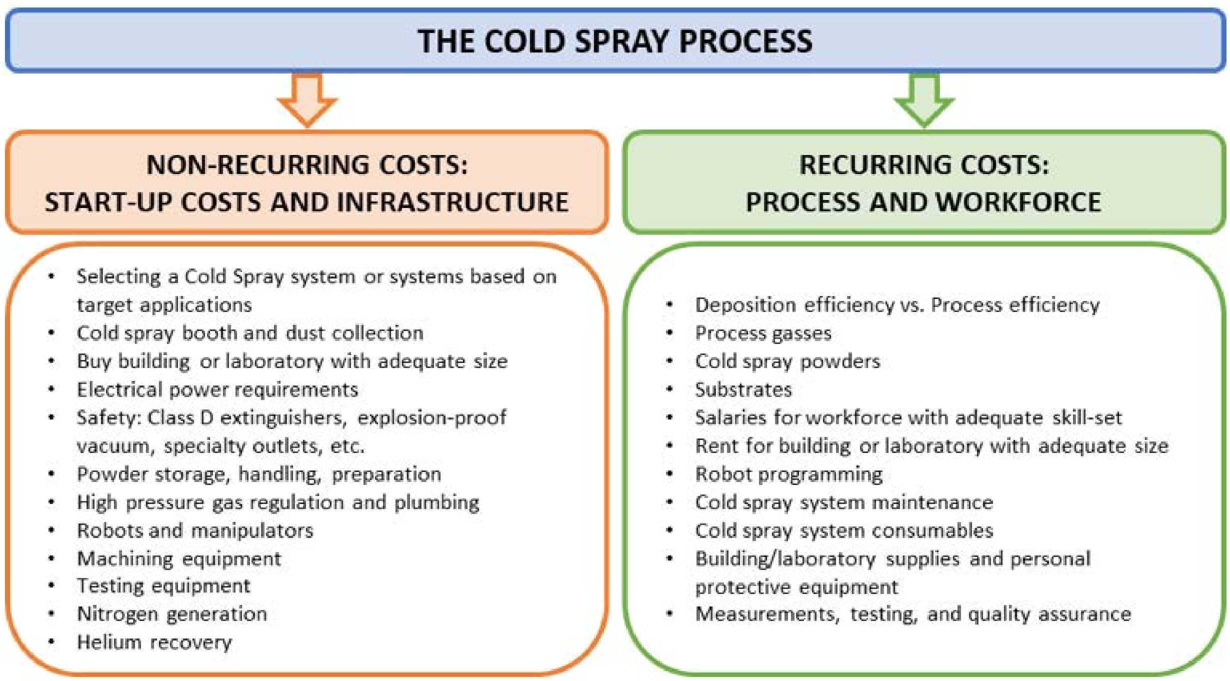

Figure 2.9. Cost overview for cold spray process and infrastructure [27]

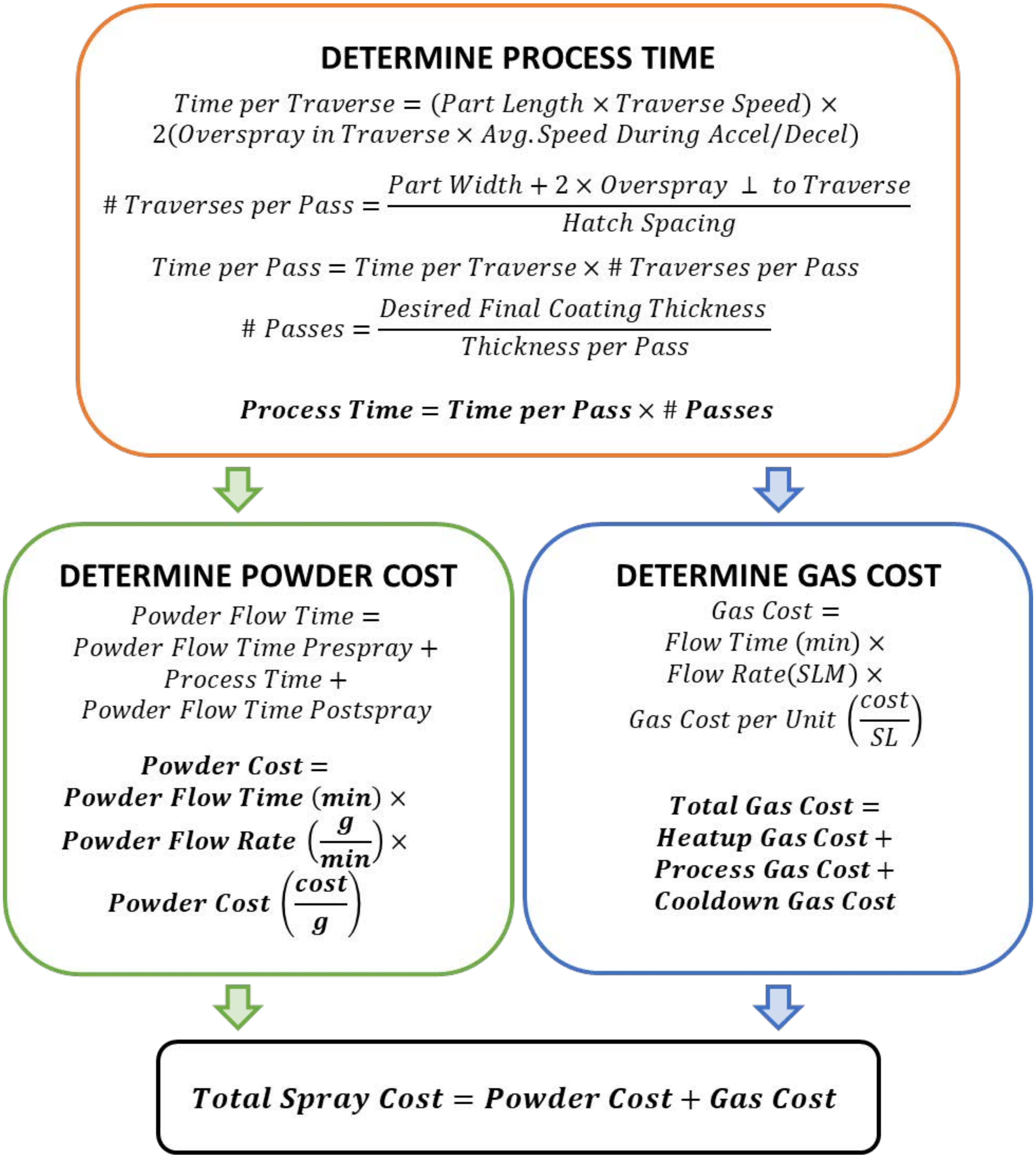

Figure 2.10. Calculations for estimating cost from powder and process gas usage [27]

2.4.1 Cost Analysis of Cold Spray Hybrid Approach

The cost of cold spray deposition is a function of the part geometry, application, and required material properties. These variables determine the powder and gas to be used for the coating. In general, helium is the most expensive component at a cost of $0.55 per cubic foot (STP) of helium used. In order to provide a baseline cost estimate for spraying 6061 powder the test specimen geometry for this research was used to generate a cost per volume of coating. On average, 630 cubic feet of helium were used to produce each cold spray specimen. Powder usage was calculated by multiplying the powder flow rate by the total spray time. A traverse speed of 400 mm/s was used on the 5" (H) x 1" (W) specimens, with a 15mm allowance for overspray. The process time was roughly 30 minutes to complete a single specimen. Process time can be optimized depending on part geometry and robot path planning. Process efficiency is defined as the mass of powder deposited divided by the total mass of powder sprayed. Process efficiency is helpful in quantifying costs of powder sprayed during heating, robot travel inefficiencies, or overspray. Table 2.2 shows the five cost factors accounted for in the total cost calculation. As mentioned previously, helium is the main source of the manufacturing cost accounting for over 90% of the total cost.

Table 2.2. Cost of Cold Spray Consumables for Specimens

Consumable	Amount Used	Cost ($ per unit)	Total Cost per Spray
Heater	10.5 kWh	$0.10/kWh	$11
High Pressure N_2	180 ft^3	$0.04 ft^3	$8
High Pressure He	1768 ft^3	$0.55 ft^3	$972
6061 Powder	0.4 lbs	$130/lb	$52
Wrought aluminum	5 in	$0.264	$1.32
		Average	$1035

In the context of a production manufacturing environment, utilizing cold spray to produce a 5" long T-channel with a 0.125" square rib would be prohibitively expensive.

Applications where cold spray excels, both functionally and economically, are repair of high dollar value parts and large part geometries [3, 28]. The larger the physical size of the part, the larger the impact cold spray has on material and machining cost savings. An example would be a large cylindrical shell that requires rib stiffeners to be placed a defined distance apart to increase the buckling resistance. The normal process for such a part would be to procure a forging with enough material on the inner diameter to account for the thickness of the ribs. Forgings are costly and the thicker material requirement often requires hand forgings which tend to have lengthy lead times. A possible avenue to save on costs associated with material and machining would be to start with a thinner cylinder and cold spray the rib features onto it. Finish machining may need to done to produce features such as threaded holes; however, it would require significantly less machining overall than its forged counterpart.

Theoretical part dimensions were chosen to analyze cold spray's viability as an additive manufacturing option. A 33" long cylindrical shell with final dimensions of 21" outer diameter, 20.25" inner diameter and 1" square rib stiffeners every 10" was used to estimate material and machining savings. For the case of machining from a forging, a forging with OD of 21.5" and ID of 17.75" would be required - allowing for 0.250" machining from each surface. A cold sprayed substrate would only need to be 21.5" outer diameter and 20.25" inner diameter, already a material savings - by weight - of 240 lbs. Cold spray costs were estimated by utilizing the same cost analysis method as above in Table 2.2. A 1" square rib sprayed onto the 20.25" inner diameter requires 61 cubic inches of material to be sprayed onto the cylinder. Assuming a rib every ten inches of shells brings the total material required to 183 cubic inches, or roughly 18 lbs of aluminum powder. By scaling the cost in Table 2.2, the total cost to spray 18 lbs of aluminum powder would be about $45000, or $15000 per rib. Equation 2.5 represents the volume of material for the rib stiffeners. Equation 2.6 is a weight calculation for a representative forging that would need to be ordered to account for rib thicknesses in a traditional machining operation. Equation 2.7 is the weight calculation for the forging for a hybrid approach with ribs added using localized cold spraying. The difference between the two weights represent not only material savings, but machine time as well. Forgings can also have long lead times (6-9 months) associated with them. Using stock material with cold sprayed features could provide significant schedule savings in addition to reducing material waste. Cold spray would eliminate the need to machine away over 200 lbs of aluminum. Given the high cost of helium, an avenue to reduce the financial burden of using cold spray is to employ the use of a helium recovery booth system. A relatively new technology, helium recovery, enables the user to recapture roughly 80% of the helium that would otherwise be expended during the cold spray process. Generally accounting for over 90% of the cost, recovering 80% of the helium would result in a huge reduction in operating costs and produces a viable path to using cold spray in a manufacturing environment. For reference, the specimens fabricated for this paper would have cost $265 to produce rather than $1035.

$$\text{Rib Volume} = \pi * (ID) * Rib_h * Rib_w \tag{2.5}$$

$$\pi * (21.5^2 - 17.75^2)/4 * L * .1lb/in^3 = 372lbs \tag{2.6}$$

$$\pi * (21.5^2 - 20.25^2)/4 * L * .1lb/in^3 = 132lbs \tag{2.7}$$

2.5 Johnson-Cook Plasticity Model

The Johnson-Cook plasticity constitutive model has been used to model several different materials and is a simple approach for modeling post-yield material behavior [29–31]. Johnson-Cook was chosen to model the plasticity of the specimens for several reasons:

- Ease of implementation into Abaqus' plasticity material model,
- Modeling efforts commonly use Johnson-Cook in works describing post-yield material behavior,
- Simple implementation when ignoring strain rate and temperature effects for quasi-static test conditions, and
- Ability to optimize material parameters based upon empirical testing data

Johnson-Cook plasticity was implemented in the finite element analysis of the four-point bend testing to model the post-yield behavior of the specimens. Equation 2.8 shows the complete equation for a Johnson-Cook plasticity material model.

$$\sigma = [A + B(\epsilon_{pl})^n][1 + Cln(\frac{\dot{\epsilon_{pl}}}{\dot{\epsilon_{ref}}})][1 - (\frac{T - T_{ref}}{T_m - T_{ref}}^m)] \tag{2.8}$$

Where A, B, n, C, and m are all material parameters that are determined by experimental data. A is the material yield strength, ϵ_{pl} is equivalent plastic strain, m is the thermal softening coefficient, and T_{melt} is the melting temperature of the material. B and n describe the strain hardening behavior of the material. C is the coefficient for strain rate effect. For this research, strain rate and thermal effects were ignored since tests were quasi-static (10^{-2} s strain rate) and conducted at room temperature. The simplified form (Eq. 2.9) is the form used in Abaqus to model the plasticity of the cold sprayed aluminum powder with strain rate and temperature effects omitted. An additional benefit of utilizing Johnson-Cook was the ability to take empirical tensile test data for the cold spray powder and fit the stress-strain curve data to produce the aforementioned material parameters. Initially, parameters were used from literature for initial modeling efforts [29]. Once tensile test data is collected, the updated parameters can be input into the model to obtain a more accurate representation of the testing results. The simplicity of the Johnson-Cook model also allows the material parameters from this research to be implemented in future analyses to predict behavior of the 6061 powder and substrate in different geometric configurations.

$$\sigma = [A + B(\epsilon_{pl})^n] \tag{2.9}$$

Chapter 3
Experiment Procedure and Methodology

3.1 Introduction

The goal of this research is to demonstrate the capability of leveraging cold spray in a hybrid additive manufacturing process for creating a part of equivalent strength to one machined from wrought aluminum bar stock. This chapter covers the overall experimental design of the research, the specifics of the cold spray process used, and an outline of testing and analysis methods used to assess the performance of the cold sprayed structures.

3.2 Cold Spray System

The aluminum 6061 coatings were deposited using a Gen III Hybrid High Pressure Additive/Subtractive Cold Spray Manufacturing System, fabricated by VRC Metal Systems, Rapid City, SD. The CS system is located at the Penn State Applied Research Laboratory. The feedstock powder was deposited using helium as the main process gas. Nitrogen was used for heating before transitioning to the helium, reducing the amount of helium used and thus the cost of the sprays. A VRC nozzle, NZL0071, was used for all sprays. The NZL0071 is a 1.75x5-173 nozzle, signifying a 1.75 mm throat, 5mm exit, and 173 mm length.

3.3 Cold Spray Parameters and Verification

Cold spray specimens were produced using the same wrought aluminum as the subtractive specimens to guarantee identical performance of the substrate. The use of the same wrought aluminum stock isolated the effect of the cold spray powder on test results. Spraying was conducted using the parameters outlined in table 3.1. Mechanical properties for the cold spray powder (Solvus SAAM-AL6061-G1H1) and the wrought aluminum can be seen in tables 3.2 and 3.3, respectively. These properties were used to inform modeling efforts. The powder mechanical properties were verified by performing tensile testing of a dogbone specimen made entirely of the Solvus 6061 powder.

Table 3.1. Experiment Cold Spray Parameters

Cold Spray Parameters	
Nozzle	VRC NZL0071
Powder Type	SAAM-AL6061-G1H1
Main Process Gas	Helium
Gas Temperature (°C)	425
Gas Pressure (psi)	525
Powder Flow Rate (slm)	150
Powder Feed Rate (rpm)	4
Nozzle Offset (in)	1
Traverse Rate (mm/s)	400

3.4 Cold Spray Powder

Aluminum cold spray powder was sourced from Solvus Global (Worcester, MA) using their Powders on Demand platform. The powder is categorized under Solvus' structural and additive manufacturing (SAAM) category. The powder, SAAM-AL6061-G1H1, is thermally processed to improve adhesion and material properties. Representative mechanical properties for the powder are shown in table 3.2. These properties are provided by Solvus Global and are average values expected for the 6061 powder in the as-sprayed condition. A particle size distribution (PSD) was completed on a sample of SAAM-AL6061-G1H1 using a Mastersizer 3000 Particle Size Analyzer (Malvern Panalytical, UK).

Table 3.2. Cold Spray Powder Characteristics

Geometry	Spherical
Hardness (Vickers)	86
Elongation	9 %
Yield Strength (ksi)	36
Tensile Strength (ksi)	43
Median Particle Size (D50)	35 μm

3.5 Test Specimens

Specimen geometry was chosen such that the cold spray material would significantly increase the stiffness and strength of the specimen during testing. In order to reduce complexity of the spraying and thus cost, a plate geometry of 1" wide by 0.125" thick was chosen with a 0.125" square rib stiffener. Specimens were a minimum of 4.5" long in order to have an outer span of 4". The 4" span maintained a span to depth ratio of 8, which allowed Euler-Bernoulli's beam theory to be applied to the geometry [32]. Equations 3.1-3.3 were used to estimate the stiffness of the plate with and without the stiffener to verify that the rib has an appreciable effect. The second moment of area (Eq. 3.2) of a 0.125" thick by 1" wide plate was calculated to be $1.6e{-}4$ in^4 while the plate with the rib stiffener had a section modulus of $4.1e{-}4$ in^4 an increase of 145%. The 145% increase in stiffness by the addition of the rib was deemed an acceptable representation of a stiffening feature and this geometry was used to compare wrought and cold sprayed specimens in a four-point bending test setup.

$$y_c = \frac{bt^2 + t_w d(2t + d)}{2(tb + t_w d)} \tag{3.1}$$

$$I_{xx} = \frac{b}{3}(d+t)^3 - \frac{d^3}{3}(b - t_w) - A(d + t - y_c)^2 \tag{3.2}$$

$$S_{xx} = I_{xx}/y_c \tag{3.3}$$

3.5.1 Wrought Aluminum Specimens

Specimens were all manufactured from wrought 6061 aluminum bar stock - 1" wide by 0.250" thick - purchased from McMaster-Carr Supply Company, Cleveland, OH (Appendix A.1). Mechanical properties can be seen in table 3.3. Wrought aluminum specimens were machined using a Bridgeport mill. Specimens were first machined flat on the base by facing off .005" using a 1/2" end mill. The part was then flipped over to guarantee the top and bottom surfaces of the specimen were perfectly parallel. The rib was machined into the part using a 1/2" end mill with a 1/16" corner cut radius (P/N 30855A65, McMaster-Carr Supply Company, Cleveland, OH). The use of the end mill with a built-in radius eliminated the need to use a ball end mill for a secondary cutting operation; thus, improving the repeatability of the machining operation and ability to consistently locate the radii for the root of the T-channel. The basic form of the specimens produced was a 4.5" long T-channel. The flange of the specimens was 1" wide by .125" thick with a rib 0.125" wide by 0.125" thick, cross-section view show in figure 3.1.

Table 3.3. Al 6061-T6511 Mechanical Properties IAW ASTM B221 [33]

Ultimate Tensile Strength (ksi)	41.7
Tensile Yield Strength	38.3
Elongation	14.5 %

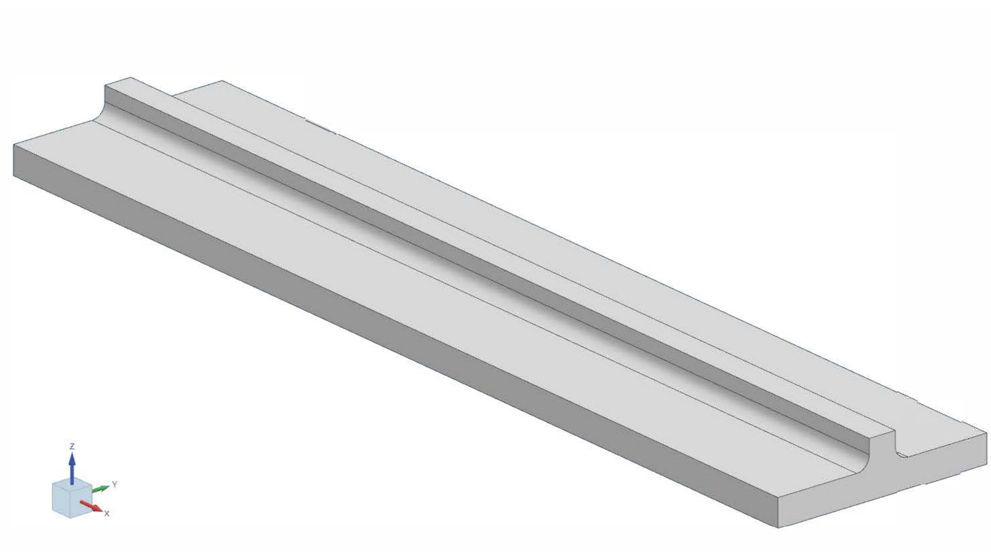

Figure 3.1. Isometric view of subtractive manufacturing specimen geometry

3.5.2 Cold Spray Specimens

Cold spray specimens were manufactured from the same bar stock as the traditionally machined specimens. Specimens were serialized using the naming convention used internally at ARL PSU, 'V0000'. The four numbers following the 'V' are a chronological identifier i.e. V2280 was the subsequent specimen sprayed after V2279. All CS information is linked to the specimen ID and allows for accurate record keeping. Sections were created from the bar stock using a circular saw to cut substrates to the proper length (4.5"). Each substrate was scoured with a Scotch-Brite pad on the side to be cold sprayed in order to interrupt the oxide layer and roughen the surface. The substrates were then cleaned with isopropyl alcohol and wiped down. These steps ensure the surface is in pristine condition which promotes better adhesion between powder and substrate. In Figure 3.2, the red section indicates cold sprayed material while the gray is the substrate (wrought aluminum 6061). For the cold sprayed specimens, a 0.050" thick layer of cold sprayed material was left on the specimens to provide a smooth transition for the radius-ed edges. Omitting the 0.050" layer could potentially induce delamination of the coating at the feathered edges of the radii - during either machining or four-point bend testing. The additional benefit of this technique was that the interface between substrate and cold spray material was located closer to the neutral axis of the part. Close proximity to the neutral axis mitigates the amount of stress the interface experiences under a bending load.

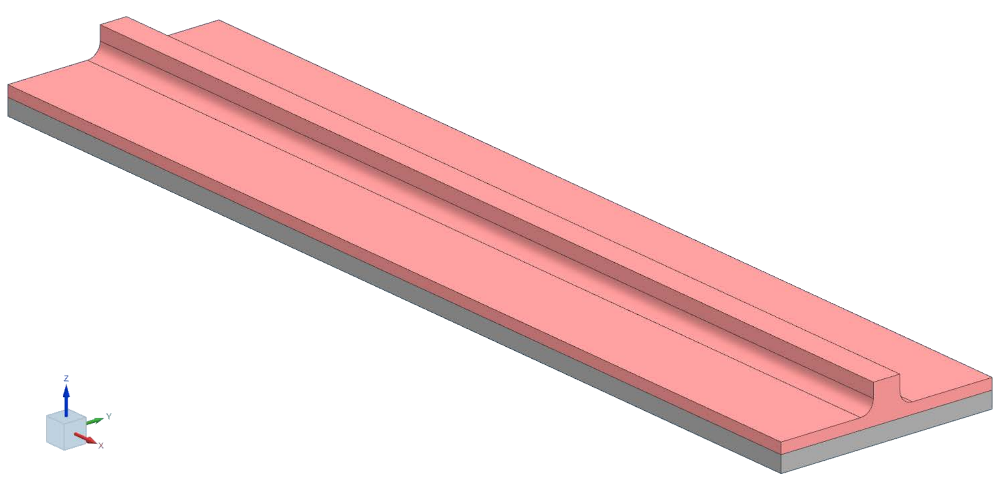

Figure 3.2. Isometric view of cold sprayed specimen geometry

3.6 CS Coating Metallography

3.6.1 Specimen Imaging Prep

Imaging specimens were sectioned using an IsoMet 1000 precision sectioning saw (Buehler, Lake Bluff, IL), equipping with a MetLab (Niagara Falls, NY) 177.8 mm (7”) diamond wafering blade. Sectioned specimens were then mounted in a MetLab epoxy-hardener mixture (7.5:1 resin to hardener ratio) to form a 1.25" diameter mold around the specimen. The mounted specimen was placed in a Struers (Cleveland, OH) CitoVac vacuum impregnation unit for 25 minutes at 2000 psi. The CitoVac removes air bubbles from the epoxy resulting in an optically clear casting. Specimens were then removed from the CitoVac and let cure for 24 hours. Cured specimens were wet ground using a LECO (St. Joseph, MI) GPX300 with 320, 600, and 1200 grit SiC grinding discs and deionized water as the lubricant. Specimens were ground for 30 seconds at each grit level. Final polishing was completed using $3\mu m$, $1\mu m$, and $.05\mu m$ polishing liquids for 15 seconds, 15 seconds, and 3 minutes respectively.

3.6.2 Optical Microscopy

Optical microscopy was completed using a VHX-7000 microscope from Keyence Corporation of America (Itasca, IL). The coating interface and porosity measurements were made using Keyence’s imaging software. Specimen V2279 was arbitrarily chosen and a .500" section was taken off the end for imaging of the CS coating prior to testing. An image of the interface was stitched together from four separate images taken at 50x magnification. Images were taken at 200x, 500x, and 1000x magnifications with porosity measurements occuring at the 500x magnification. Porosity calculations were completed using Keyence software. Given that all specimens were sprayed using the same parameters, specimen V2279 was assumed to be a representative coating for all cold sprayed specimens. Optical microscopy was also completed on specimen V2282 post-testing. Two sections were taken, one at the midpoint and one outside of the 4" span width. The two locations were chosen to provide a comparison between a region that experienced maximum stress and a region that experienced no stress (outside of the span).

3.6.3 Scanning Electron Microscopy (SEM)

SEM was completed using an Apreo 2 Scanning Electron Microscope, Thermo Fisher Scientific (Waltham, MA). SEM was conducted on four-point bend specimen V2282, tensile testing specimen V2657, and SAAM-AL6061-G1H1 cold spray powder. Circular back scatter (CBS) was the detection method for all SEM images collected. When using CBS, contrast in the images indicates a difference in atomic number. This technique works well due to the difference in atomic number between aluminum (13) and a void (0). Magnifications ranged from 500x to 5000x for the collected images. Energy-dispersive spectroscopy (EDS) was completed on a SEM sample of the interface. EDS provides elemental analysis of a SEM sample. AZtecLive (Oxford Instruments, Concord, MA) was used to complete the EDS.

3.7 Material Testing

Ultimately, two different tests were conducted to determine the viability of the hybrid approach for manufacturing stiffened aluminum structures. The first test method was four-point bending conducted on the T-channel specimens described in Section 3.5. Strain, force, and displacement were collected during each test and provided the basis for comparing cold sprayed specimens with wrought specimens. Secondly, tensile testing was completed in accordance with ASTM E8 [34]. Properly characterizing the mechanical properties of the powder in the as-sprayed condition gave a direct comparison to existing 6061-T6 data for elongation, yield strength, and ultimate strength.

3.7.1 MTS Landmark Servohydraulic Load Frame

Data was collected using two different systems. Force and displacement data was collected from the MTS TestSuite TW Elite Software that is included with the MTS Landmark Load Frame. For the four-point bend testing, crosshead speed was set at 0.039 in/min (1 mm/min) for the duration of the test [35]. The load cell installed on the load frame was MTS Model 661.20H-03, calibrated in accordance with ASTM E4 [36]. The force and displacement data were collected at a frequency of 20 Hz. The four-point bend tests were concluded once the displacement of the actuator reached 0.250". This was mainly due to the rollers beginning to move outward as the specimens began to deform significantly.

3.7.2 Strain Measurement Data Collection

The strain data was collected independently from the load frame data via a National Instruments 9237 and a single strain gauge (Micro-Measurements, P/N C4A-13-125SL-120-39P) located at the midpoint of the specimen on the tensile side of the beam. Strain data was valid up to 3% (maximum reading of the gauge). The strain data served as validation of the force and displacement data provided by the load frame. The strain data was also used to verify the accuracy of the FEA model in predicting the stresses in the specimen (The strain gauges are general purpose, linear gauges used for stress analysis. The gauge length was 0.125 in and the gauges were oriented parallel to the longitudinal axis of the beam on the tensile side of the specimen.) Figure 3.3 shows the location of the gage on the specimen and the orientation relative to the four-point test fixture. Strain data was collected at a sampling frequency of 1000 Hz and down-sampled to 20 Hz to synchronize with the force and displacement data.

3.7.3 Cold Spray Tension Testing

Tensile specimens were sprayed using the same parameters as the four-point bend specimens - parameters shown in Table 3.1. The specimens were machined by Acura-Cut

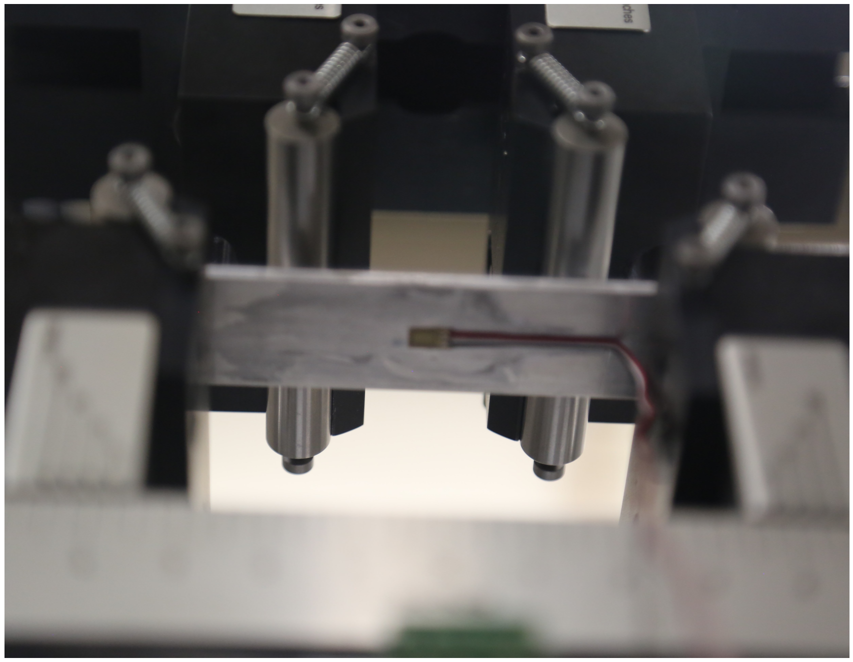

Figure 3.3. Strain gage test setup location on specimen

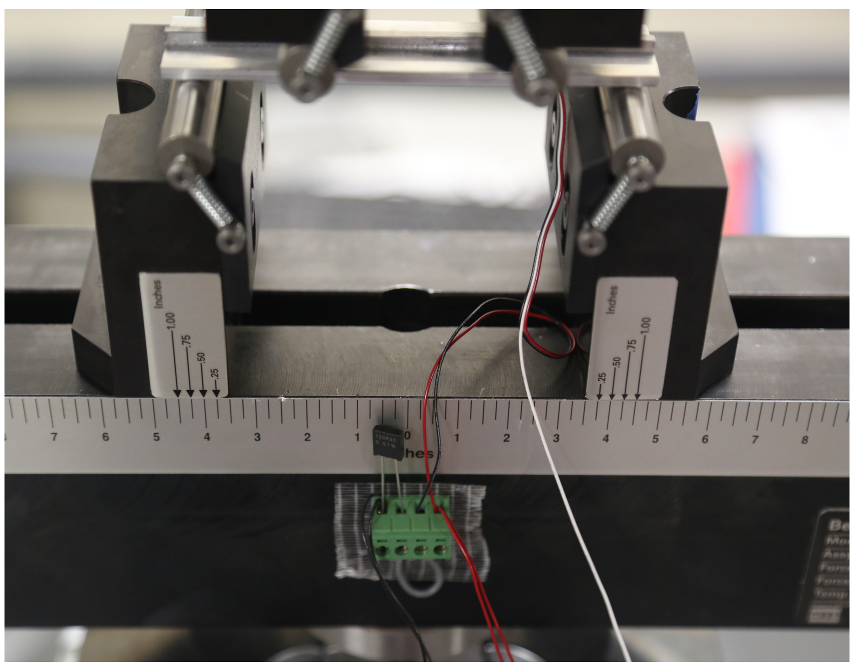

Figure 3.4. Wiring setup for strain gage data collection. 120 ohm precision resistor used to complete quarter bridge.

(Pleasant Gap, PA) via wire EDM in accordance with ASTM E8. Specimens were 0.125" thick and 0.250" wide with a gauge length of 1.25" - part drawing included in Appendix

B for reference. Specimens were sanded longitudinally (tensile testing direction) with 120, 240, and 400 grit sandpaper, sequentially, to remove the EDM recast layer and any surface flaws from the specimens. A strain rate of 0.015 in/in/min was used in order to determine the elastic modulus in accordance with ASTM E111. Given the specimen's gauge length of 1.250", the tensile tests were completed using a crosshead speed of 0.01875 in/min. A single test was used to determine the modulus rather than three individual tests in the linear elastic region [37]. A 1" axial extensometer from MTS (P/N 634.11E) was used to measure strain.

3.8 Finite Element Modeling

A finite element analysis (FEA) was completed to model stress response of the specimen and attempt to reproduce experimental results. Abaqus 2022 was used for all analyses. The four-point bend setup was modeled in quarter symmetry to allow for more detailed meshing of the T-channel specimen. Figure 3.5 shows the quarter and full symmetry models. The full symmetry model is shown solely to provide context for how the quarter symmetry model relates to the full geometry. Rollers were constructed from hardened steel and thus were modeled as rigid bodies. Rigid bodies reduce computation time by ignoring the stress states within the rigid body. The model was run in the same manner as the tests - controlled displacement of the crosshead to a known value. The lower roller was held fixed with all degrees of freedom set to zero. Displacement for the top roller was limited to 0.250". A secondary analysis step was run to simulate the crosshead (top roller) returning to zero. This step allowed the part to be unloaded and display the plastic deformation predicted by the FEA. The FEA plastic strain values were then compared to the values of the strain gauges post-test.

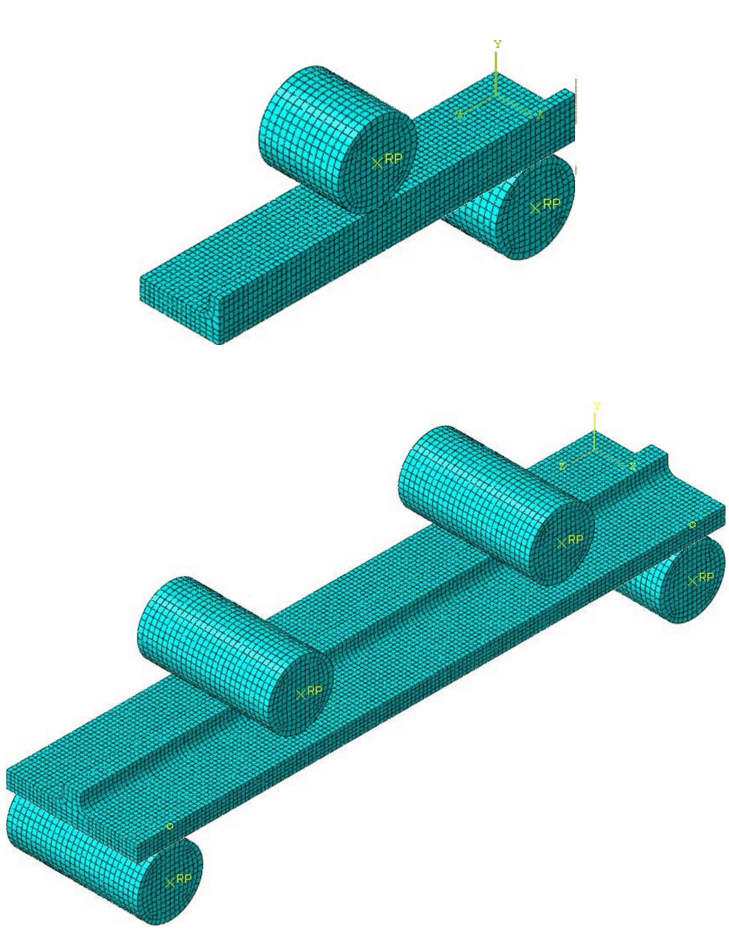

Figure 3.5. Quarter and full symmetry models of the four-point bend test setup

Table 3.4. Mesh properties for finite element analysis

Part	Element Type	Global Seed Size (in)	Number of elements
Roller	C3D20R	0.038	2340
T-Channel	C3D20	0.020	20792

Chapter 4
Results and Discussion

4.1 Introduction

Results of the experimental procedure are outlined in this section. Topics covered:

- Coating and process parameters verification,
- Optical imaging before and after four-point bend testing,
- SEM on powder, tensile specimens, and four-point bending, specimens
- Tensile test results,
- Four-point bending results, and
- FEA results.

4.2 Coating Characterization and Imaging

4.2.1 Process and Parameter Verification

For this specimen geometry, a pass is defined as the traversal of the nozzle laterally across the 1" width of the substrate. The desired coating thickness for aluminum 6061 is 0.005-0.006" per layer of cold spray deposited onto the substrate. A 1" x 1" substrate was prepped and sprayed using the parameters shown in Table 3.1. The substrate was coated with six passes, the first with the nozzle at 45 degrees and the remaining five orthogonal to the substrate. After spraying, the specimen was measured to determine the amount of aluminum powder deposited onto the substrate. Measurements were taken in each quadrant of the 1"x1" to obtain an average thickness. Coating thickness was found to be 0.005" ± 0.0001 per pass which was within the objective range, measurements shown in Table 4.1.

Table 4.1. Cold Spray Powder Characteristics

Sample	Pre-Coat (in)	Post-Coat (in)	Coating (in)
1	0.2485	0.2797	0.0312
2	0.2489	0.2800	0.0311
3	0.2487	0.2790	0.0303
4	0.2487	0.2798	0.0321
Average	0.249±0.0001	0.280±0.0006	0.031±0.0006

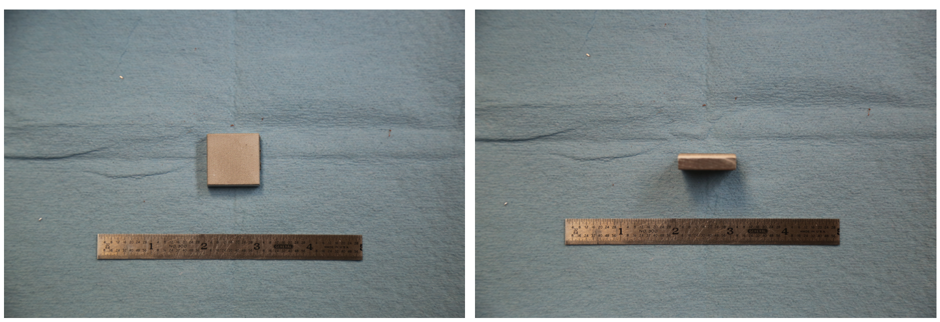

Figure 4.1. Coating thickness verification on 1" x 1" substrate

4.2.2 Powder Imaging

Samples of the Solvus SAAM-AL6061-G1H1 powder were characterized via scanning electron microscopy (SEM) and a PSD. Figure 4.2 shows the morphology of the powder. While generally spherical, elongated particles are present throughout the samples and smaller satellite particles can be seen around the larger particles. Figure 4.3 displays an ideal spherical particle. The particles below the spherical particle are good examples of a satellite particle (lower left) and oblong particle shape (lower right). Figure 4.4 displays the internal microstructure of a particle.

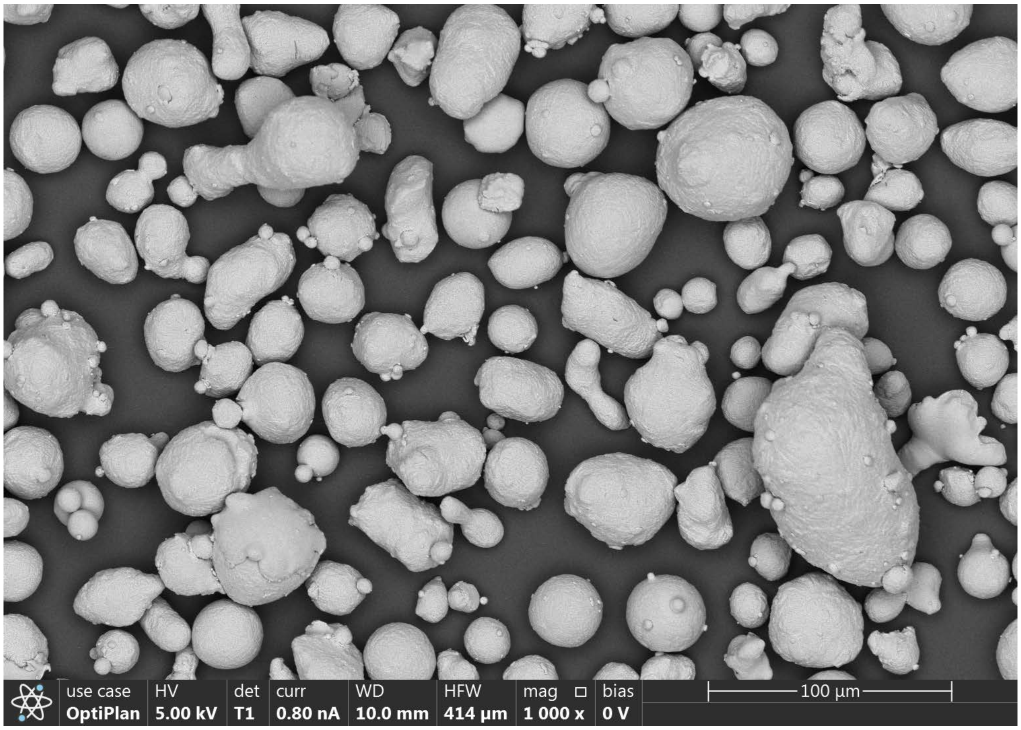

Figure 4.2. Powder morphology of SAAM-AL6061-G1H1 sample. Powder is generally spherical with some elongated particles

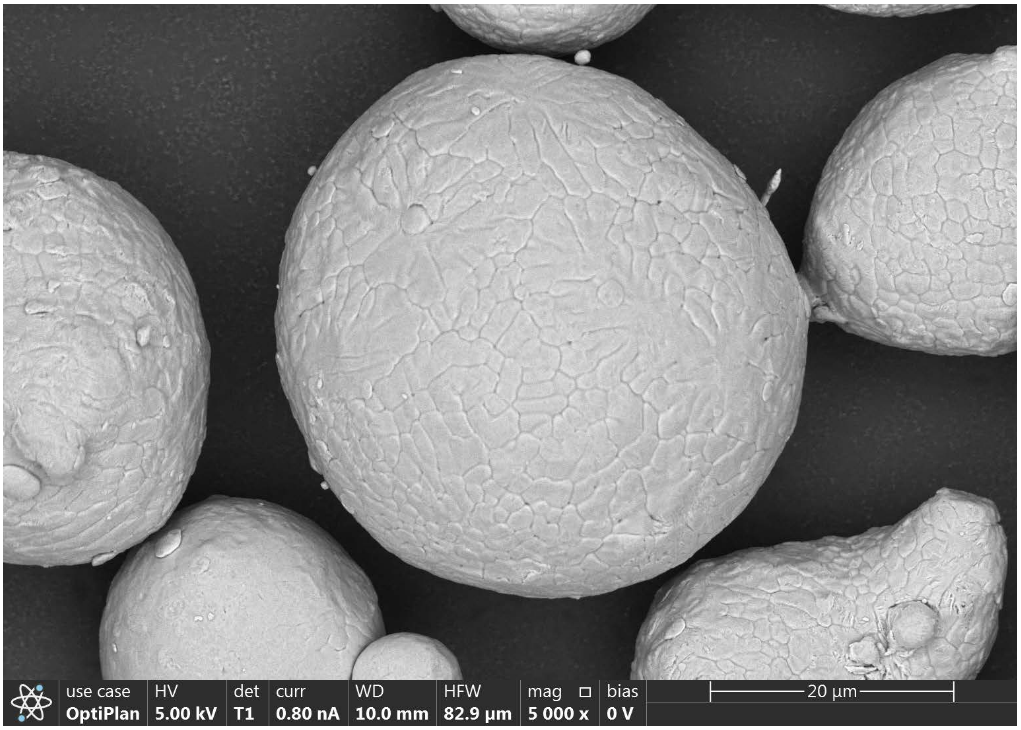

Figure 4.3. Surface microstructure of an ideal spherical particle.

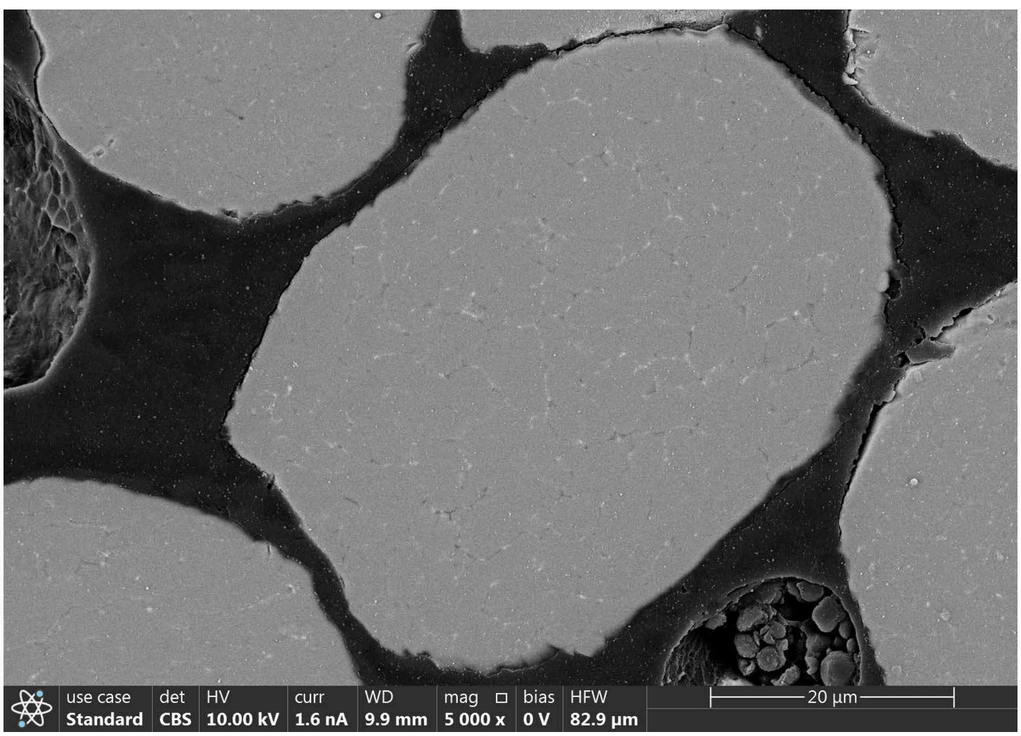

Figure 4.4. Internal microstructure of single particle captured in epoxy and polished.

4.2.3 Particle Size Distribution (PSD) Results

Results of the PSD in figure 4.5 are within the range provided by Solvus for their SAAM-AL6061-G1H1 powder. A comparison of Solvus's size distribution and the PSD results is shown in Table 4.2. The results of the PSD are in agreement with the specifications provided by Solvus.

Table 4.2. Particle size distribution comparison between Solvus specification and PSD analysis.

	D10 (μm)	**D50** (μm)	**D90** (μm)
Solvus	14 to 26	34 to 42	53 to 80
PSD	23.9	39.1	64.0

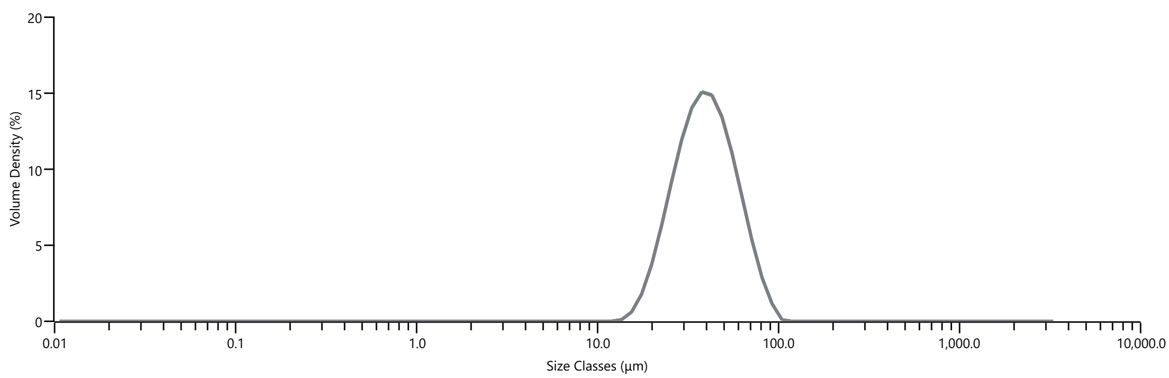

Figure 4.5. PSD of Solvus SAAM-AL6061-G1H1 powder.

4.2.4 Coating Adhesion Testing

Coating adhesion testing was completed to verify the coating bonded to the substrate. A 3"x6" dolly plate was sprayed with a 0.060" thick coating. The same powder and process parameters displayed in Tables 3.1-3.2 were used to spray the coating onto the dolly plate. ASTM D4541 "Standard Test Method for Pull-Off Strength of Coatings Using Portable Adhesion Testers" specimens have four failure points - test fixture, adhesive, coating, and substrate. In general, if the coating is correctly applied to the substrate, the specimens should fail at the adhesive. The adhesive, Solvay FM-1000, has a tensile strength of roughly 10 ksi, significantly less than the expected 35 ksi yield for the aluminum powder and substrate. Due to the limitations of the adhesive's strength, these tests only identify extremely poor performing coatings - the assumption being that the coating and substrate under test have higher yield strengths than the adhesive. The benefit of the test is that it is quick and simple to setup and verifies that there are no serious issues with the spray parameters, metal powder, or substrate preparation process. Results from the ASTM D4541 tests are displayed in Table 4.3. All four dolly plate specimens failed at the adhesive - as shown in Figure 4.6 - indicating a quality interfacial bond between the coating and substrate.

Table 4.3. ASTM D4541 Adhesion Test Data

Sample Number	Coating and Substrate Material	Rate of Pull (psi/sec)	Max Stress (psi)	Std Dev (psi)
V2278-1	Al 6061	200	12195	
V2278-2			12033	
V2278-3			11393	
V2278-4			12616	
		Average Stress	12059	508

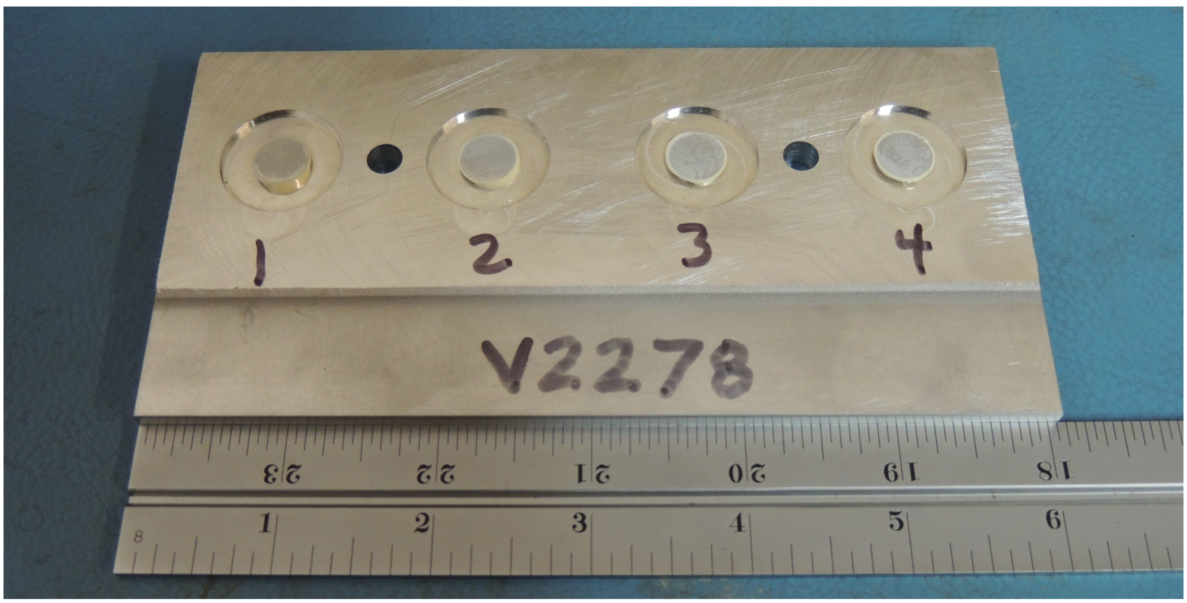

Figure 4.6. Dolly plate post-testing IAW ASTM D4541.

4.2.5 Interface Imaging

A section of V2279, the first specimen produced, was imaged to investigate the quality of the coating and the interface with the substrate. Figure 4.7, displays the cold spray-substrate interface in its entirety. The images were taken on a Keyence VHX 7100 using various lenses to achieve different magnification levels. For the 50x magnification, Keyence's image processing software stitched together several images producing a full image of the interface. Figures 4.8 and 4.9 have a magnification of 200x and 500x respectively, with the latter being a magnification of porosity identified in the 200x image. Porosity was calculated using an image processing capability included with the Keyence microscope. The total area of porosity was found to be 280 μm^2, just .11% of the area of the total area in the image. Figure 4.10 offers further evidence that the coating deposited onto V2279 is uniform and adhered well to the substrate. The substrate (bottom portion of the image) appears to show more porosity throughout; however, this is an artifact of the polishing process. Since hardened precipitates of the wrought aluminum are more resistant to polishing, they often are pulled away from the material rather than polished flat. This effect, known as pullout, is expected for a precipitation hardened alloy such as 6061. The uniformity of the cold spray coating and absence of significant porosity is more evidence that the cold spray parameters used in this research produced an effective bond between powder and substrate. Given the correct parameters, a more consistent and, most importantly, mechanically stronger material can be produced from the 6061 cold spray powder. With the specimen coating characterized and its quality validated, four-point bend testing was completed on the prepared specimens.

Figure 4.7. Optical imaging of cold spray interface (specimen V2279). Particle deposition affected by edges of specimen - illustrated by "rounded" coating on either side. Interface indicated by red line. Magnification: 50x

Figure 4.8. Optical imaging of cold spray interface (specimen V2279). Magnification: 200x.

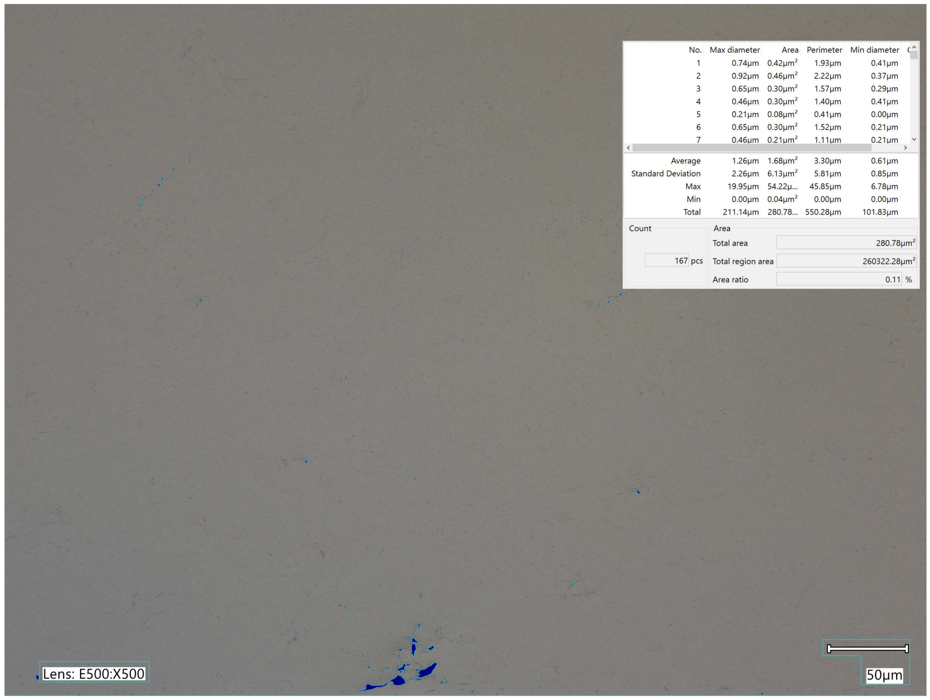

Figure 4.9. Optical imaging of cold spray interface (specimen V2279). Magnified view of the porosity circled in the previous figure. Magnification: 500x

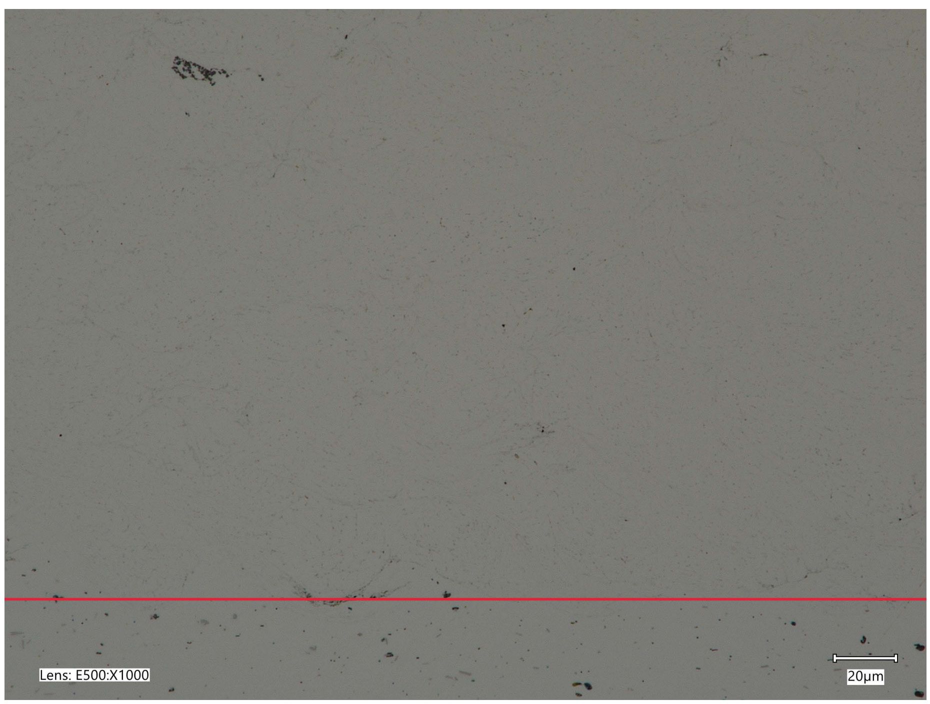

Figure 4.10. Optical imaging of cold spray interface (specimen V2279). Red line indicates interface of CS coating (top) and substrate (bottom). Magnification: 1000x

4.2.6 Powder Tensile Testing

Tensile testing in accordance with ASTM E8 "Standard Test Methods for Tension Testing of Metallic Materials" was conducted on dogbone tensile specimens composed of 100% cold sprayed material. Specimen geometry for the tensile tests can be found in Appendix B.1. Specimens had a gauge length of 1.250". Average thickness of the specimens was 0.156" and average width was 0.245". The modulus was determined from the initial data of the tests to failure, rather than the three runs specified by ASTM E111 "Standard Test Method for Young's Modulus, Tangent Modulus, and Chord Modulus". This is acceptable according to the standard as long as it is noted. The strain rate was set at 0.015 in/in/min in accordance with ASTM E111 [37]. Factoring in the gage length, the cross head speed for all three tests was 0.01875 inches per minute. Results from the tests are located in table 4.4 and the tensile data collected is shown in figure 4.11. All three tensile specimens had a similar maximum load around 1680 lbs with an average ultimate strength of 43785 psi. Average strain at break was 5.2% for the specimens, a significant reduction in the ductility expected for wrought aluminum 6061, but an expected value for cold sprayed specimens of aluminum 6061 (see Table 2.1 for comparison). This reduction in ductility highlights one of the disadvantages of the cold spray process. The plastic deformation that the particles undergo during bonding leads to a highly work hardened final state. Other research has demonstrated post-processing of samples via heat treatment as a viable way of recovering ductility but was not pursued for this study [26].

Table 4.4. Individual and averaged results from ASTM E8 tensile testing for Al 6061 cold sprayed specimens.

Specimen ID	Modulus (psi)	0.2% Offset Yield (psi)	Ultimate Strength (psi)	Strain at Break (in/in)
V2657-1	9.674e6	37255	43761	0.0507
V2657-2	9.658e6	37015	43505	0.0491
V2657-3	9.749e6	37579	44090	0.0560
Average	9.694e6±0.040	37283±231	43785±239	0.0519±0.003

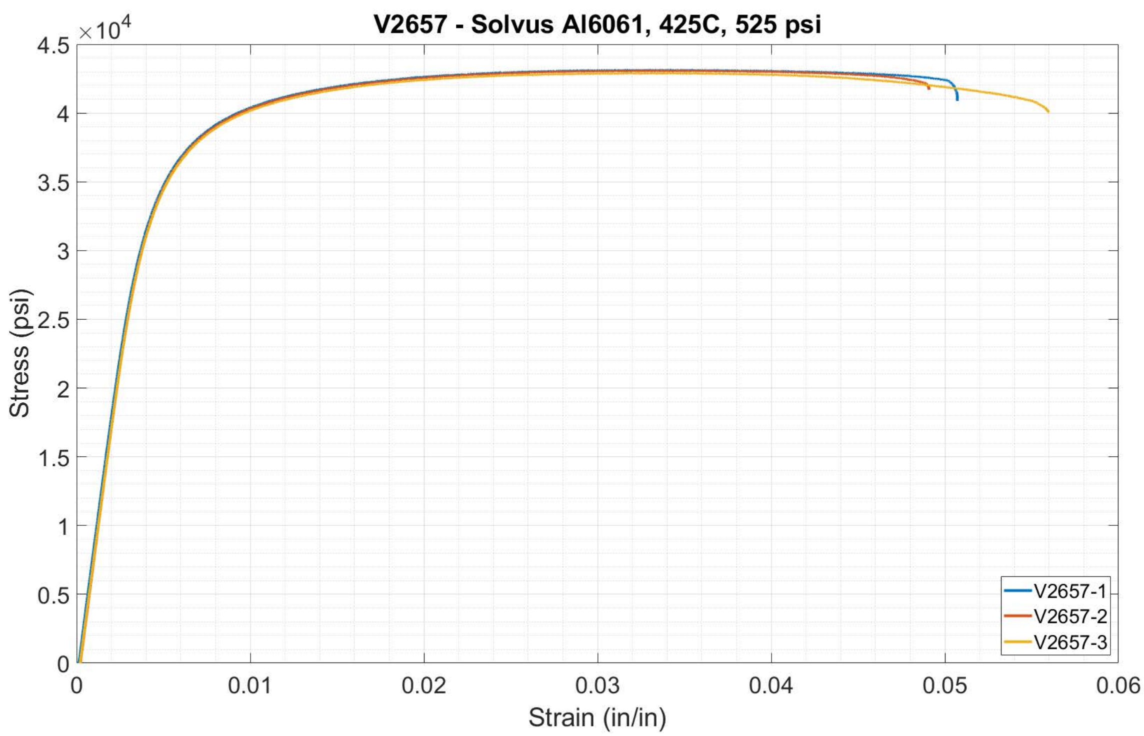

Figure 4.11. Tensile data for three specimens composed of cold spray powder to characterize mechanical properties of powder

4.2.6.1 SEM Imaging

SEM was completed on a post-test tensile specimen to image the fracture surface and the face in the width direction. Figures 4.12-4.15 show the fracture surface of the tensile specimen at various magnifications. Cold spray materials exhibit a mixed-mode failure behavior under tension where ductile failure is paired with debonding of particles. Figures 4.12 provides a macro view of the fracture surface with ductile failure is mixed with particle debonding and pullout which is shown by the voids present throughout the image. Figures 4.13 and 4.14 show more detailed views of the failure surfaces. In figure 4.14, the dark 'eyelash' above the three smooth surfaces is an indication of particle pullout. The aforementioned smooth gray surfaces indicate particle to particle debonding, due to inadequate adhesion. Figure 4.15 is a great example of the mixed failure mode of a cold spray tensile specimen. The dimpling on the left side of the image is an expected fracture surface for ductile material failure. On the right, is a potential debonding or particle pullout location where the cold spray coating was not as good. Figure 4.16 shows the bulk CS material. Porosity is present throughout the tensile specimen. Figure 4.17 is a magnified porosity location that illustrates the localized debonding that can occur without bulk failure in a CS specimen. Figures 4.18 and 4.19 reinforce the observations about porosity throughout the bulk material while showing an orthogonal view of the fracture surface. Figure 4.18 has a couple good examples of coating debonding in the lower portion of the fracture surface. Cracks are beginning to form parallel to the direction of the load being applied but they do not propagate before tensile failure. Figures 4.20 and 4.21 display a similar phenomena occurring on the edge of the part. A localized crack is formed as a result of coating failure but the crack does not propagate far enough to induce failure. Overall, SEM imaging of the tensile specimen indicated it failed as expected with a mixture of ductile failure and coating debonding.

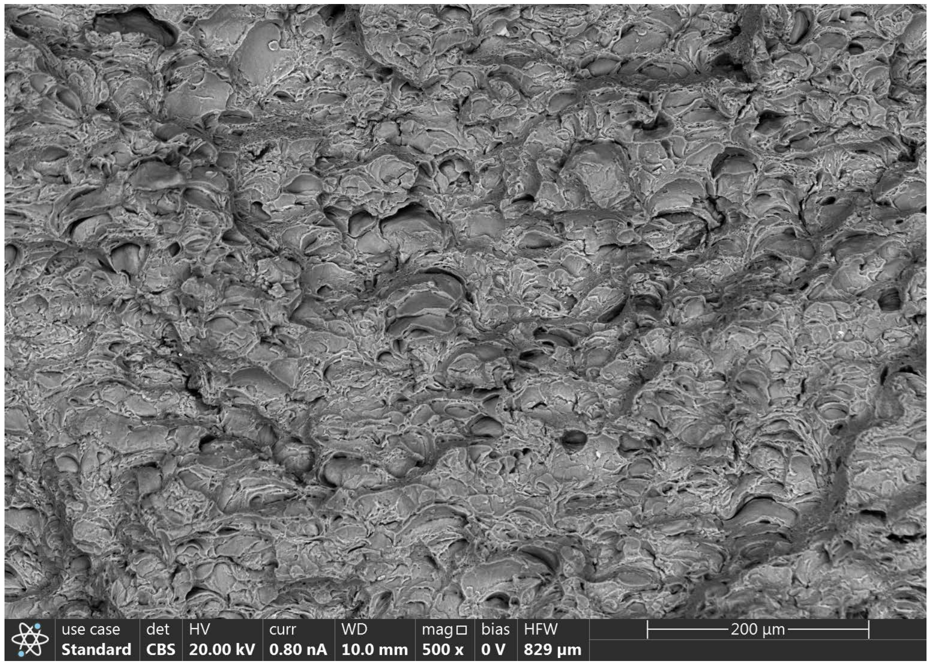

Figure 4.12. Tensile specimen fracture surface showing mixed-mode failure. Flat gray surfaces indicate particle to particle debonding while surrounding dimpling indicates ductile failure. Magnification: 500x

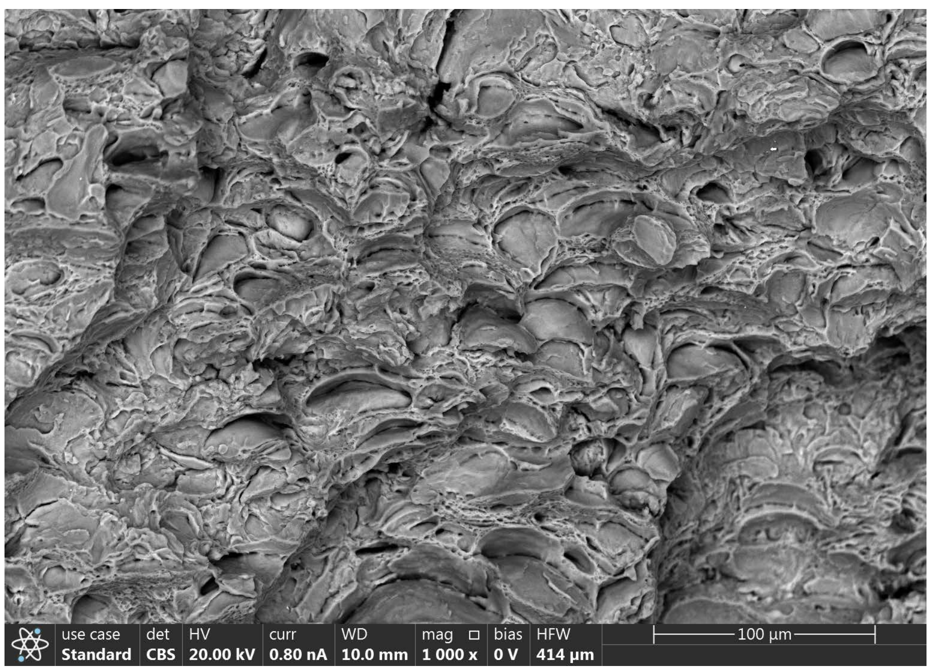

Figure 4.13. Increased magnification on a section of the previous image (1000x) showing the mixed mode fracture surface.

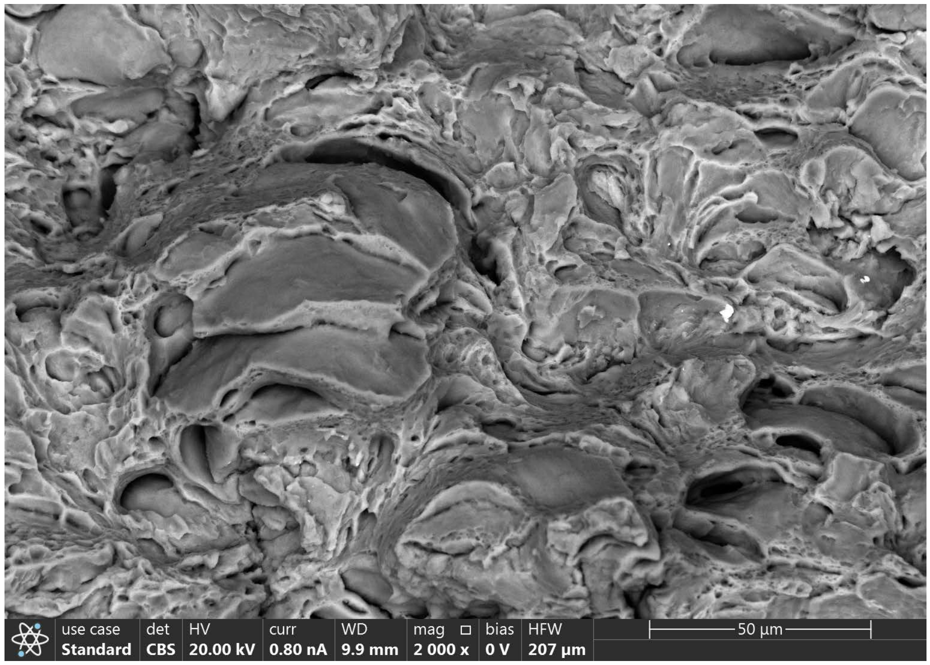

Figure 4.14. Localized area from tensile fracture surface to focus on mixed-mode failure. The three stacked flat surfaces represent particle to particle debonding while the surrounding "dimpled" areas are typical of ductile fracture surfaces.

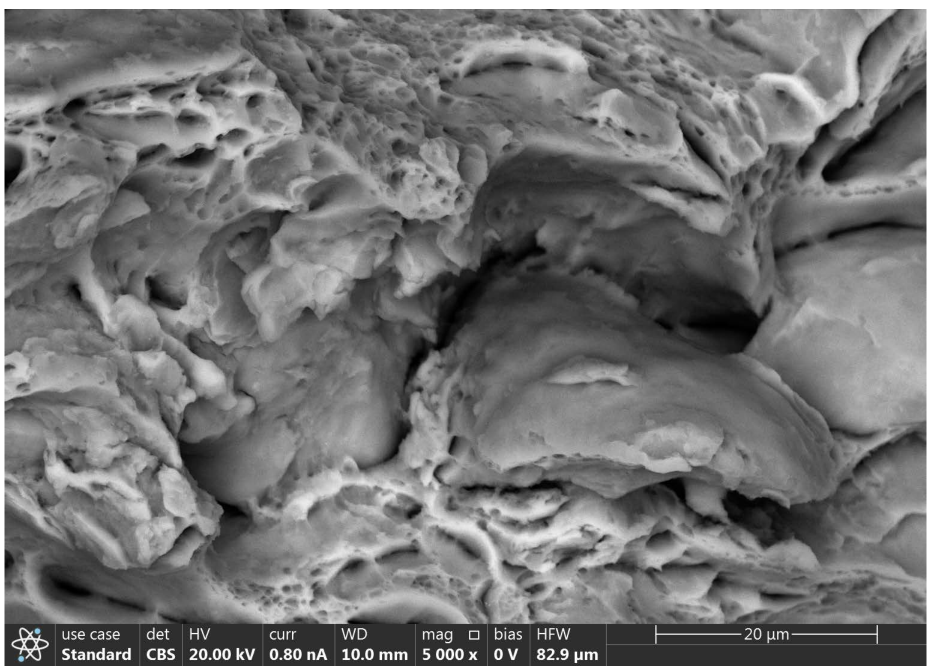

Figure 4.15. Crevice as a result of debonding between CS coating particles. Dimpling around the crevice typical of ductile fracture.

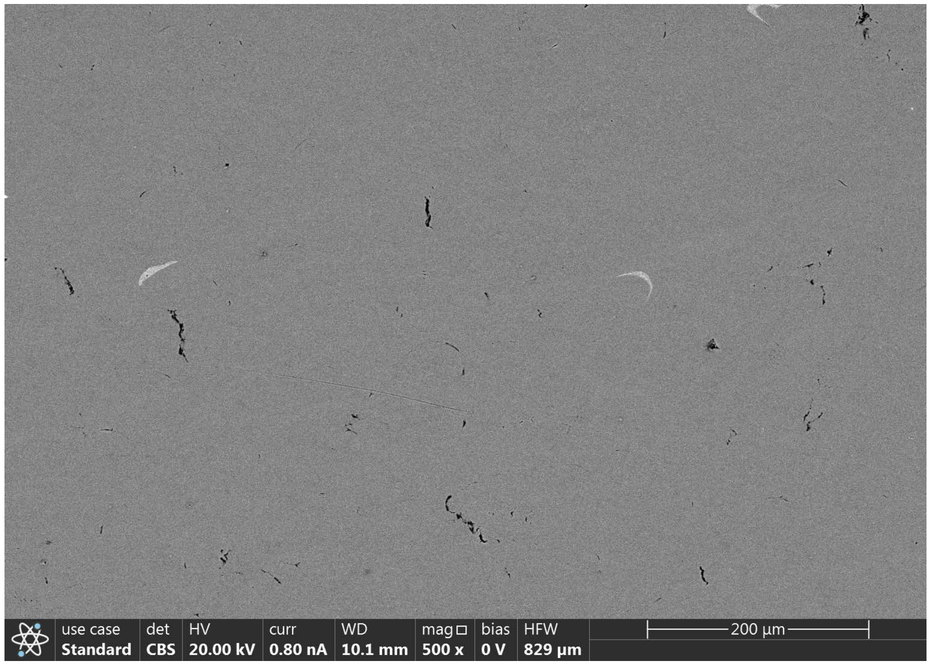

Figure 4.16. Porosity present throughout specimen indicating localized failures of coating. Increased porosity post-loading was also seen in the four-point bending specimens.

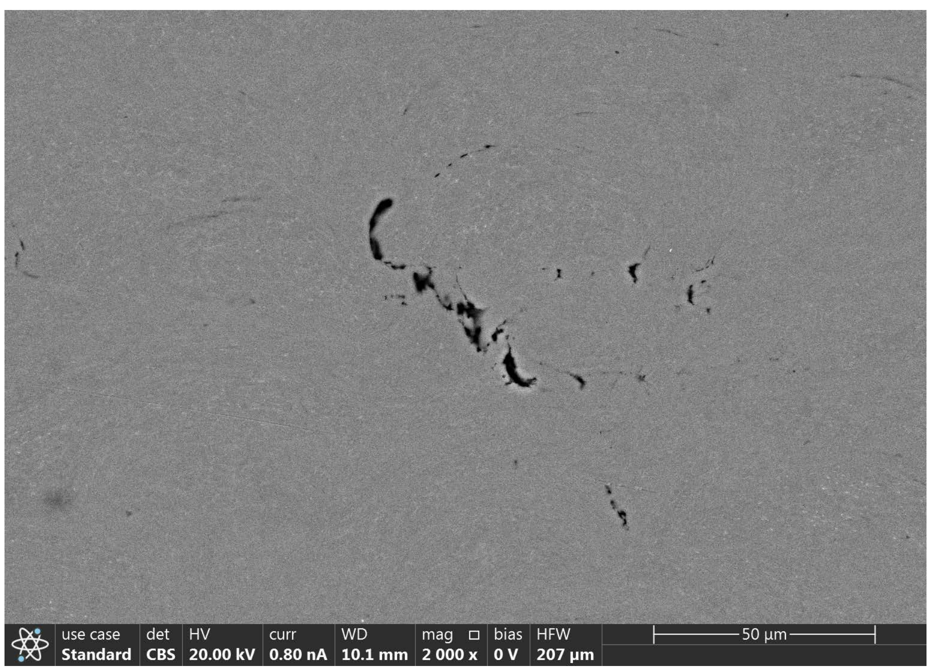

Figure 4.17. Magnified view of porosity area from the previous figure. Particle to particle separation initiated but did not result in failure of the specimen in that region.

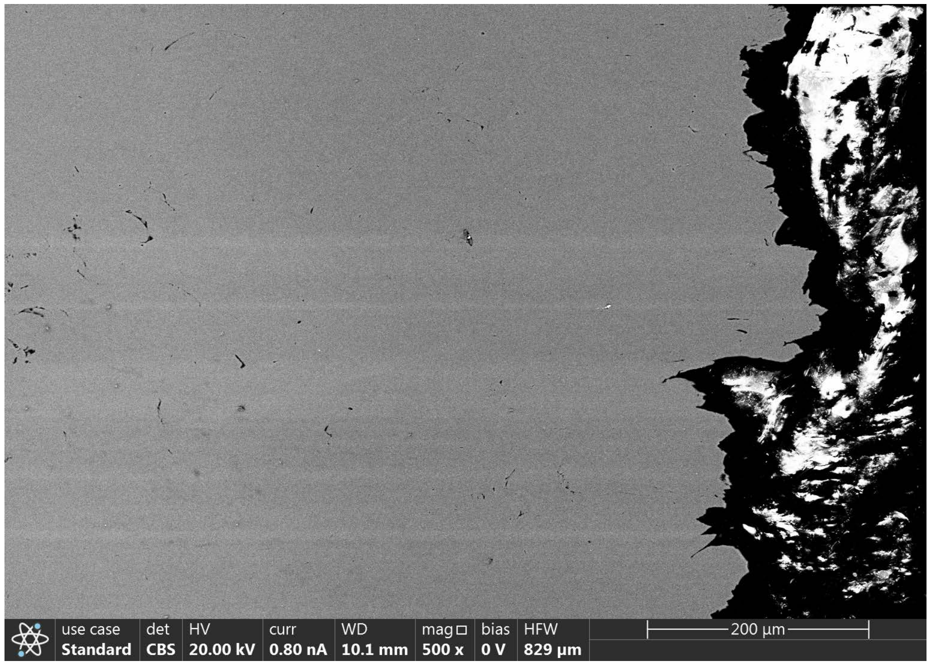

Figure 4.18. SEM image orthogonal to the fracture surface. Localized cracks present along fracture surface (tension applied from right to left).

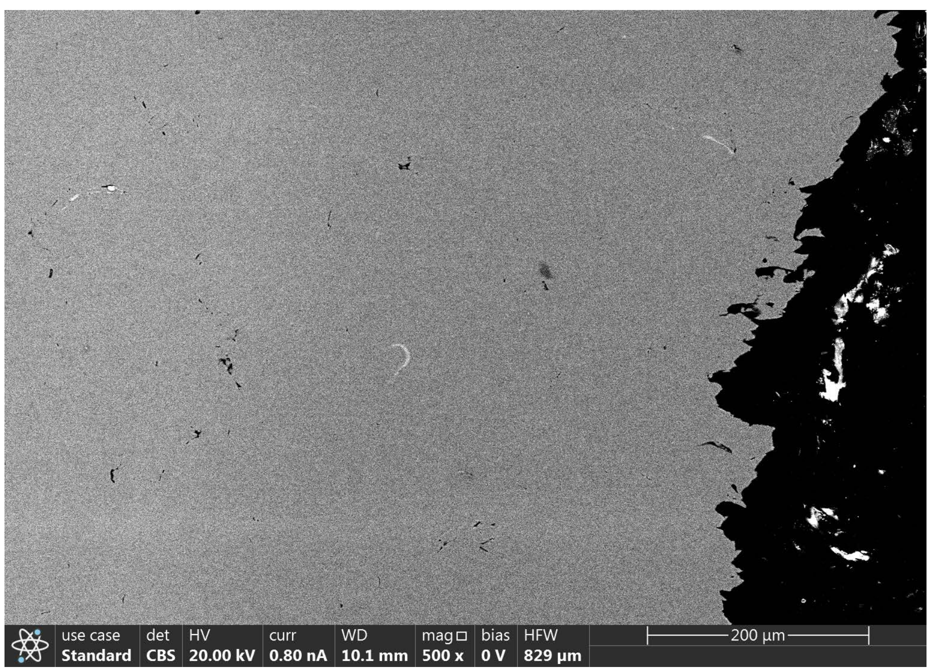

Figure 4.19. Fracture surface orthogonal to view (tension applied from right to left).

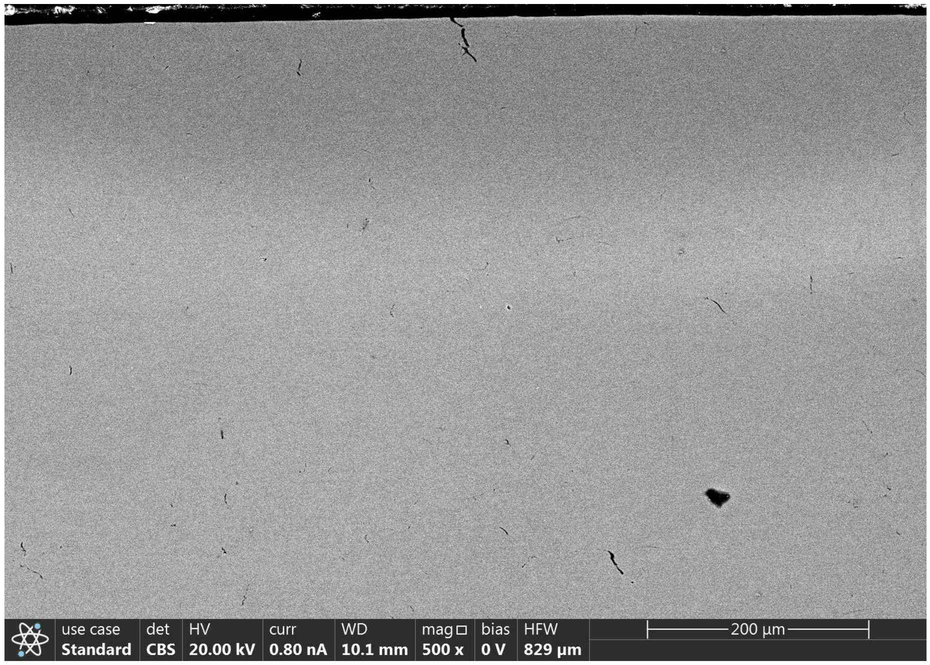

Figure 4.20. Localized crack formation on edge of specimen. Small amounts of porosity can be observed throughout the bulk material where debonding/failure initiated during tensile testing.

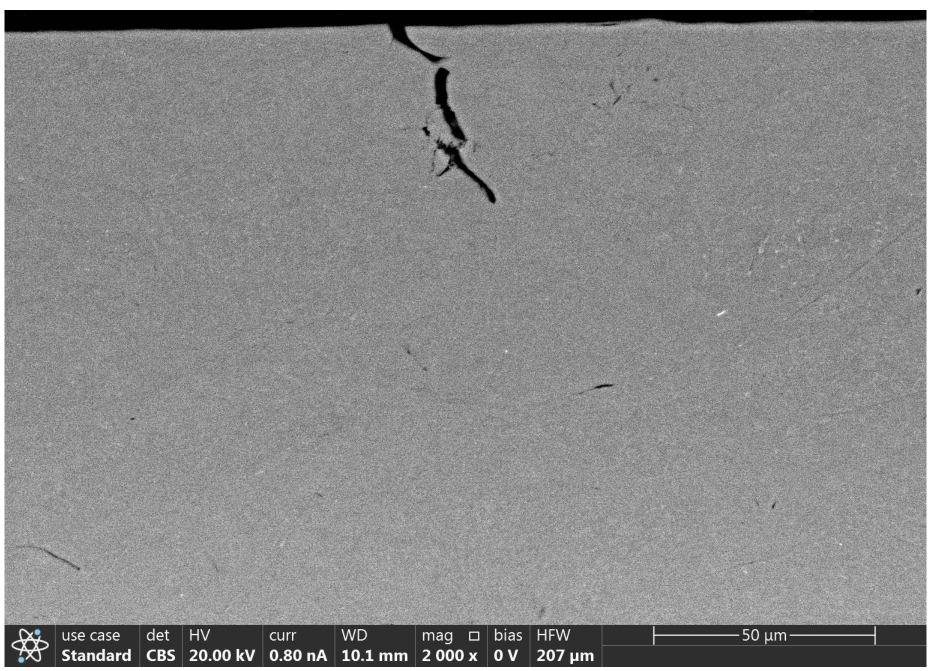

Figure 4.21. Magnified view of edge crack. Crack did not propagate and is likely a result of particle to particle debonding.

4.3 Four-Point Bend Testing

Four-point testing was completed to compare the strength, flexural stiffness, and strain behavior of the cold sprayed specimens against the wrought specimens. Table 4.5 displays the measurements taken for cold sprayed specimens prior to testing in four-point bending. The variation in length was ignored since the span was 4" for all tests and the material outside of the span does not contribute to the response and is solely to make sure the specimen does not slip off the rollers as it begins to deform. The four-point bending setup is displayed in figure 4.22. Tests were conducted until crosshead displacement reached 0.250 inches. Tests were stopped at this point to ensure the rollers would not spring outward when the specimen was deformed under loading. Roller "popout", displayed in figure 4.23, was observed on an initial checkout test and was corrected prior to conducting tests on specimens.

Table 4.5. Cold Spray Specimen Dimensions

Specimen ID	Overall Height (in)	Flange Width (in)	Web Height (in)	Web Width (in)	Length (in)
V2279	0.251	1.003	0.120	0.122	4.632
V2280	0.247	1.001	0.124	0.123	4.521
V2281	0.256	1.004	0.125	0.123	4.523
V2282	0.253	1.006	0.126	0.120	4.543
V2283	0.253	1.003	0.120	0.122	4.530

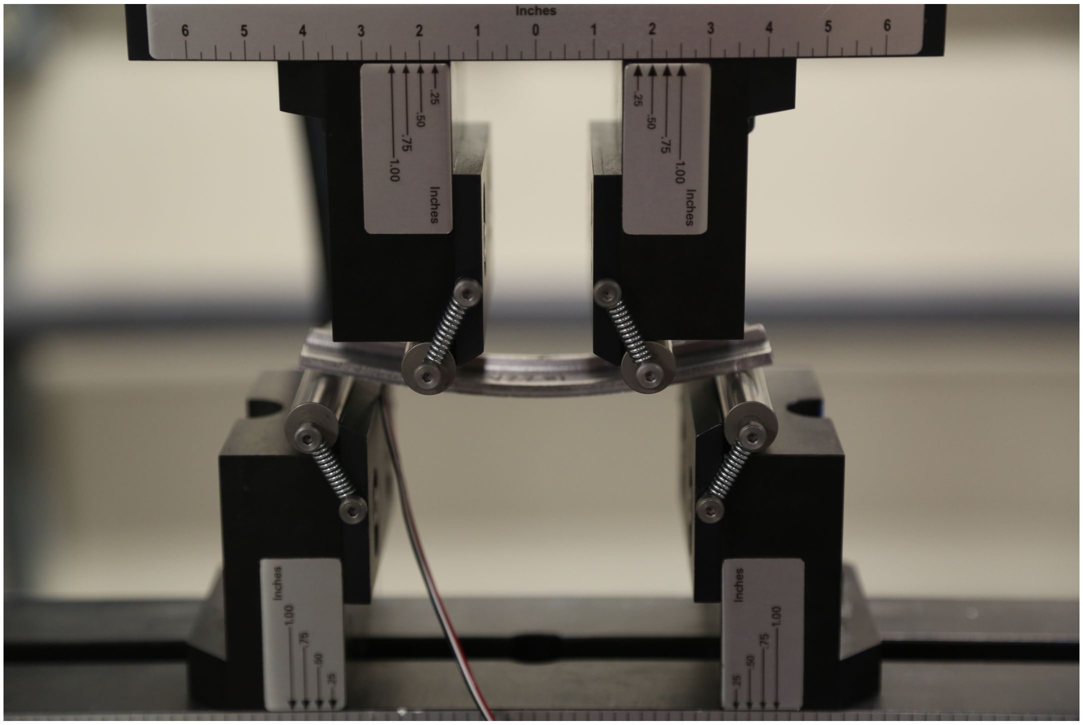

Figure 4.22. Cold spray specimen, V2281, under load in four point bend fixture.

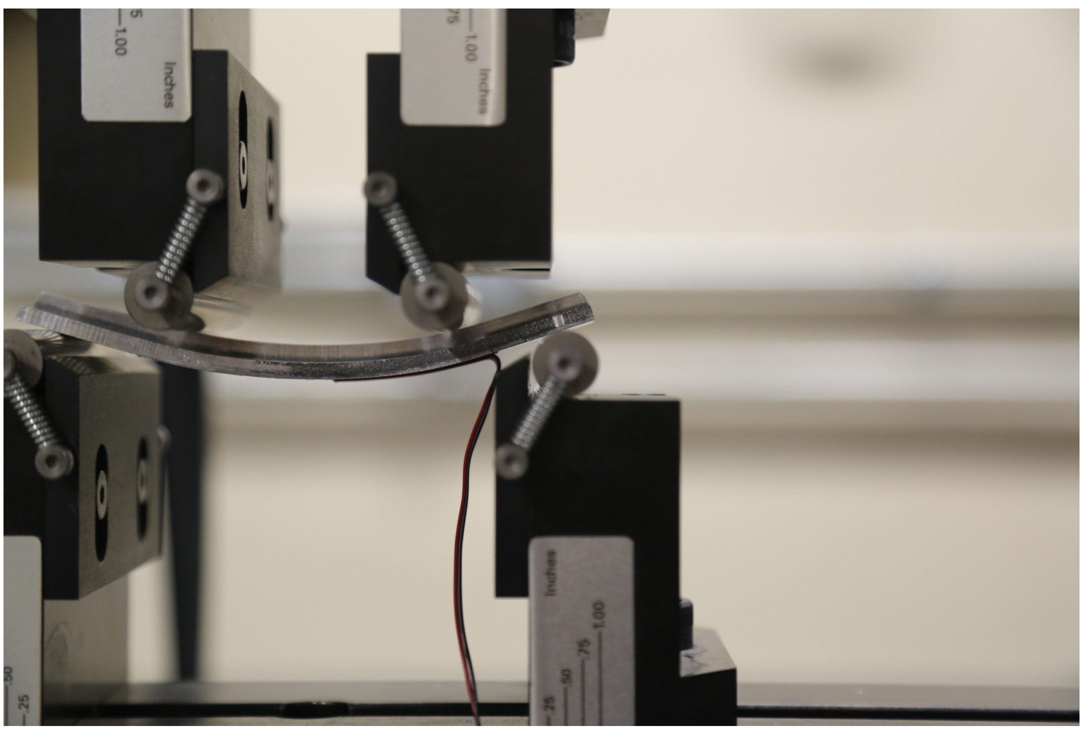

Figure 4.23. Roller separation observed during preliminary testing to gain familiarity with MTS bend fixture. Crosshead displacement was limited to 0.250" to prevent roller from springing outward while under load.

Force-displacement data of all bending tests is shown in Figure 4.24. The post-yield behavior of both types of specimens varied greatly between specimens. Two wrought specimens produced the lowest force response of all ten specimens tested. Four of the six strongest specimens were cold spray specimens. This is in agreement with the tensile data collected for the cold spray powder as the average ultimate strength was 43.8±0.24 ksi while the material certification for the wrought aluminum was 41.7 ksi. Averaged values for the cold spray and subtractive specimens are shown in Figure 4.25. The maximum values of the average force response for cold spray and subtractive were 611 lbs and 584 lbs, respectively. The cold spray specimens on average were 4.5% higher than the subtractive specimens. Qualitatively, the force-displacement curves look very similar in both the elastic and plastic regions, other than the slight increase in force response of the cold sprayed specimens.

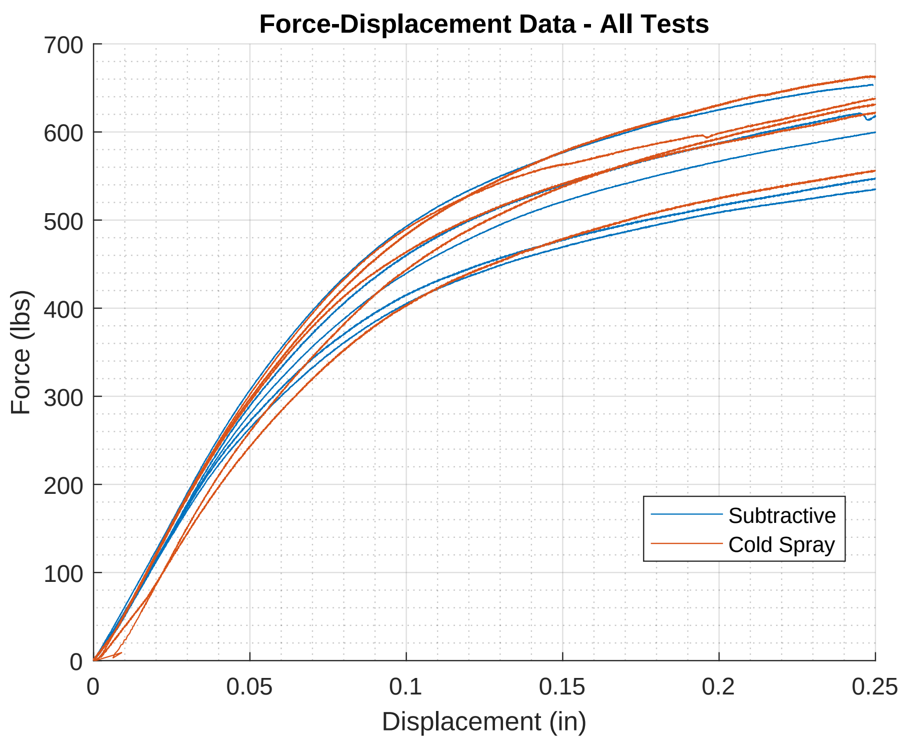

Figure 4.24. Force-displacement curves for all ten bend tests. Subtractive specimens displayed a wider distribution of force response in comparison to the cold spray specimens.

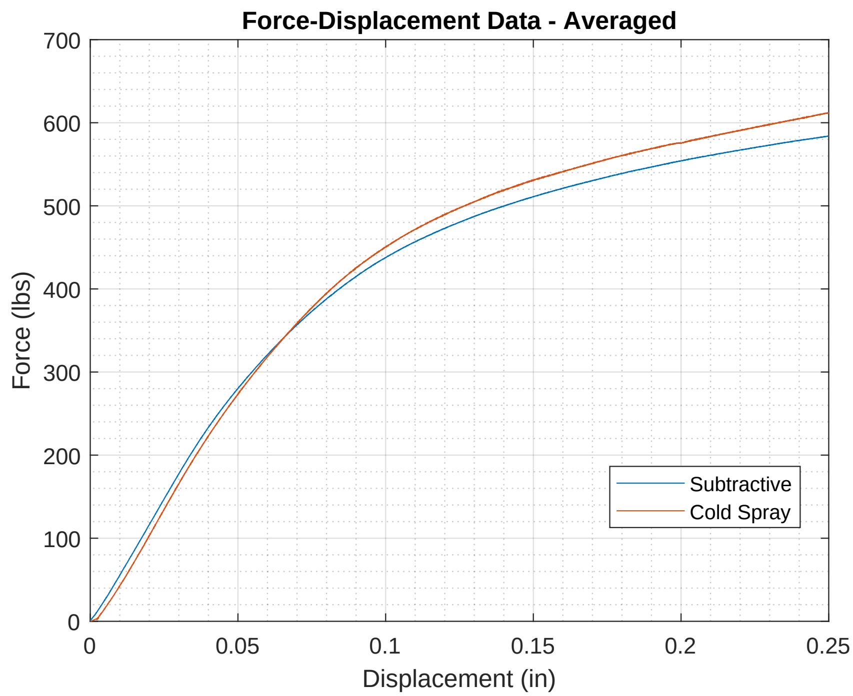

Figure 4.25. Force-displacement curves for averaged response of each specimen type. Cold spray specimens averaged a 4.8% higher load than the subtractive specimens at the same crosshead displacement.

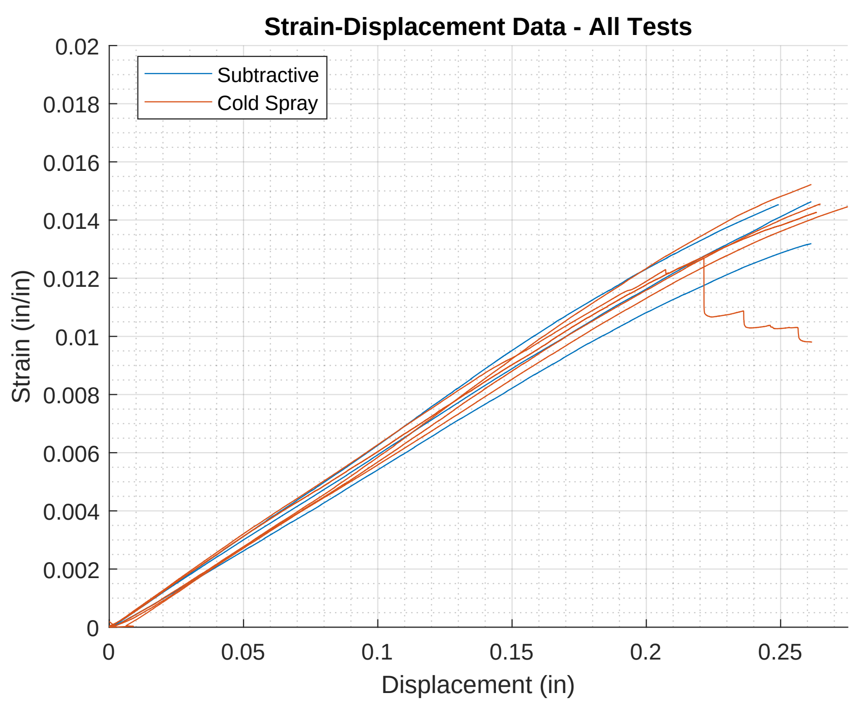

Figure 4.26. Strain data for eight of the ten bending tests. Subtractive specimens 4 and 5 experienced strain gage delamination (failure) at 9000 $\mu\epsilon$, as seen by sharp drop at 0.22".

4.3.1 Post-Test Imaging

SEM images were taken in two areas of the four-point bend specimens - the midpoint of the specimen and an area outside of the outer span. The midpoint section experiences the highest stress during a four-point bend test while the outer span should be unchanged as it undergoes no loading during a four-point bend test. For all images, the orientation of the specimen is such that it forms an upright T with the cold spray layer on the bottom and the wrought aluminum on the top. As previously mentioned in Chapter 3, specimen V2282 was used for all SEM imaging. Figures 4.27 and 4.28 show the state of the bulk CS coating and the porosity of the interface for a location outside of the outer span of the four-point bend test. These locations experienced zero loading and should be in an as-sprayed condition. Porosity at the interface is in agreement with optical images taken for specimen V2279 (Figures 4.7-4.10). The CS coating in figure 4.27 is excellent with limited porosity and small void sizes. Figures 4.29 and 4.30 display two images taken at two different locations on the midpoint specimen. Figure 4.29 is located in the center of the T-channel while figure 4.30 is located left of center along the flange. Porosity is present along the interface in both locations, however the porosity located at the center shows larger voids and potential particle debonding in localized areas. Figure 4.31 is a magnified view of a porosity location in Figure 4.30. EDS was completed on Figure 4.31. The white particulates are a combination of magnesium and iron based on the EDS results (figures 4.32-4.33). Elemental composition of the CS coating and substrate is as expected for aluminum 6061 alloy. Figure 4.34 provides an interesting comparison between the outside span and midpoint locations. The porosity is noticeably increased and the size of the voids is much larger for the bulk CS coating at the midpoint. Although the CS specimens were equal to wrought specimens under static conditions, the observed increase in porosity post-test could have implications for fatigue applications or cyclic loading. Porosity-based plasticity models that track the formation and propagation of ductile and brittle failure could be used to investigate fatigue life of the CS coating [38]. The final figure, Figure 4.35, shows a particle level image of potential particle to particle bonding as well as particle to substrate. The observed microstructure is similar to that seen in Figure 4.4, confirming the preservation of particle microstructure after bonding to the substrate.

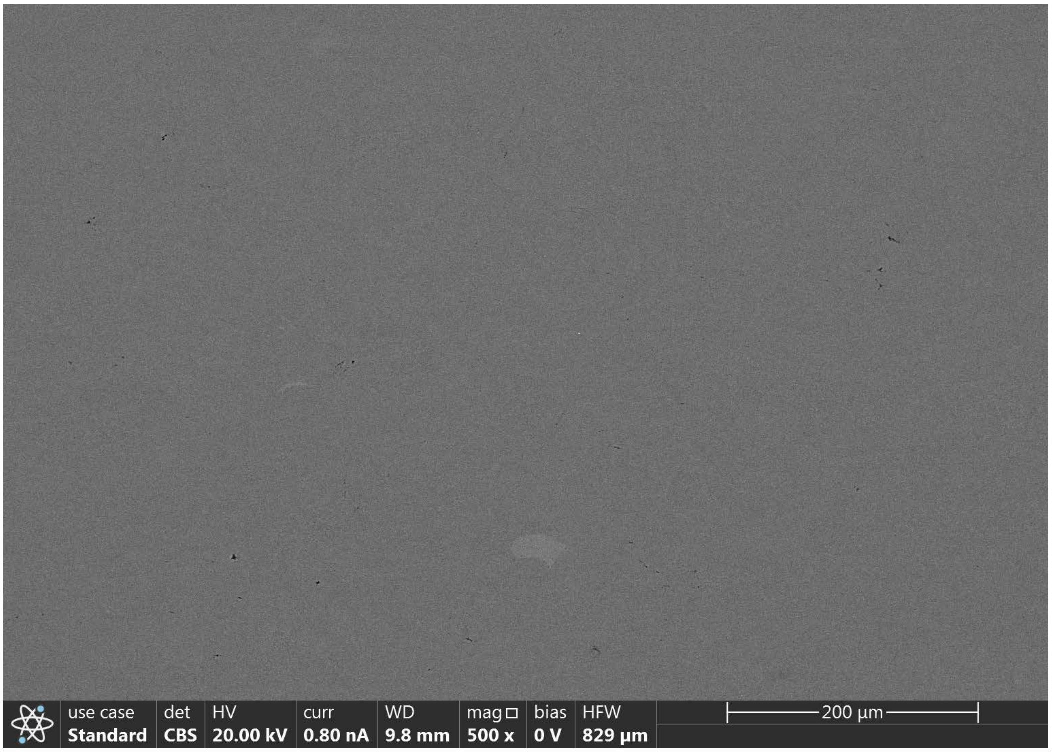

Figure 4.27. Bulk CS material outside of outer span showing a dense, consistent coating. Coating is noticeably less porous than the section inside the span that experienced the bending load.

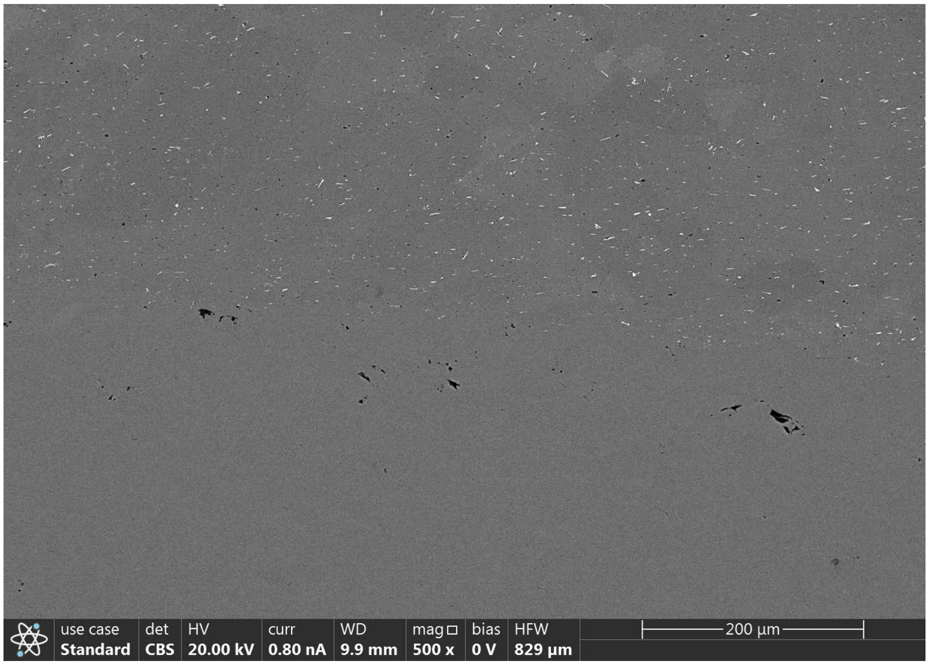

Figure 4.28. Interface at outside span location of specimen V2282. Substrate is top section with white speckling (magnesium and iron particulates based on EDS).

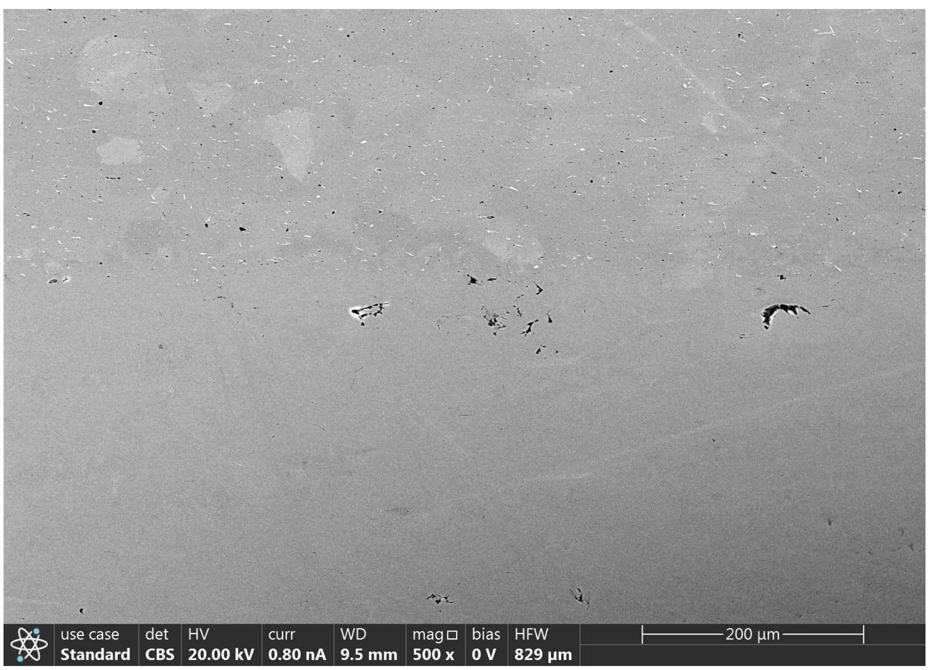

Figure 4.29. Interface of CS coating (bottom) and substrate (top) at midpoint showing large voids in CS coating. Porosity is noticeably higher than figure 4.27.

.

Figure 4.30. Interface at midpoint of specimen V2282 along the flange, left of center. Charging is present on the lower portion of the image and is due to proximity to the edge of the specimen.

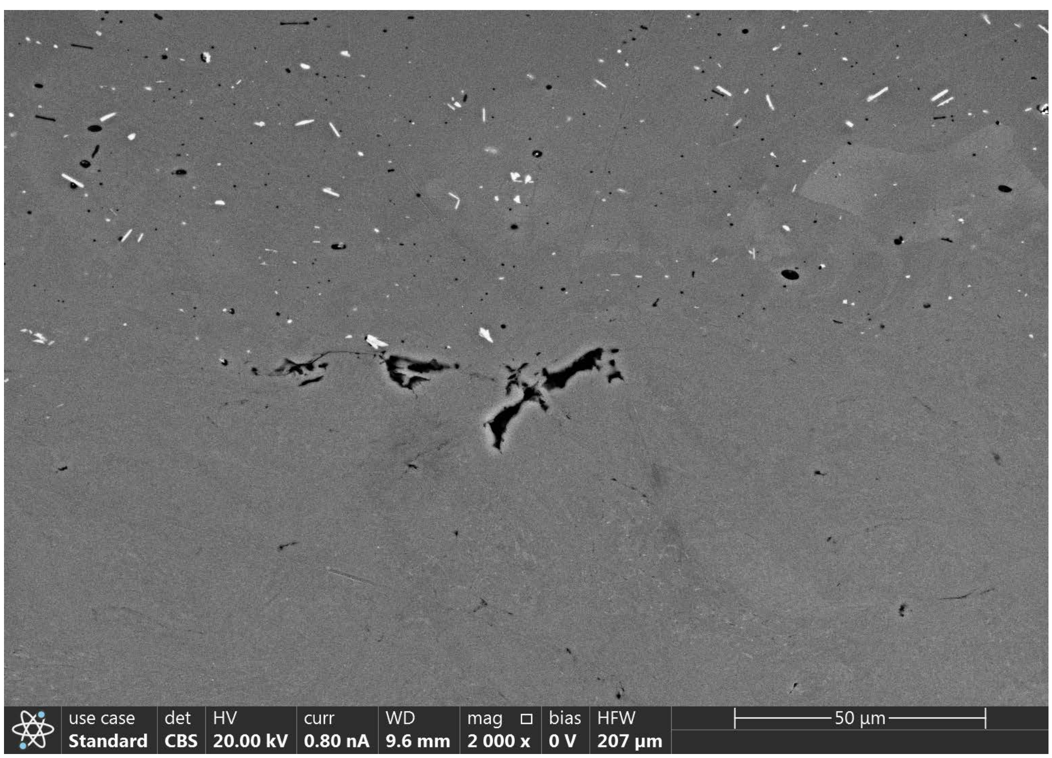

Figure 4.31. Magnified view of porosity location seen in previous figure.

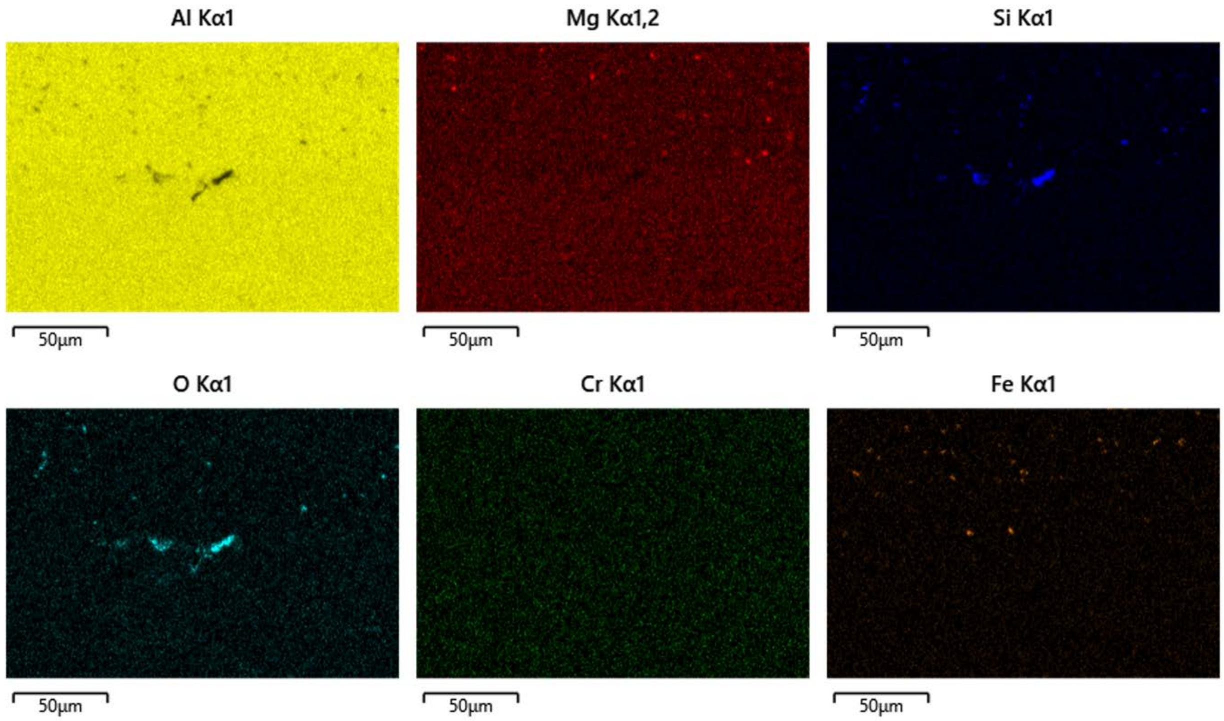

Figure 4.32. EDS results for figure 4.31 showing elements present in the SEM sample.

Map Sum Spectrum					
Element	**Apparent Concentration**	**k Ratio**	**Wt%**	**Wt% Sigma**	**Atomic %**
C	0.57	0.00569	6.17	0.11	12.82
O	0.81	0.00272	0.95	0.03	1.47
Mg	1.49	0.00987	0.81	0.01	0.83
Al	153.08	1.09949	90.96	0.12	84.13
Si	0.32	0.00256	0.58	0.01	0.52
Cr	0.07	0.00073	0.07	0.01	0.03
Fe	0.16	0.00163	0.15	0.01	0.07
Ni	0.08	0.00080	0.07	0.01	0.03
Cu	0.26	0.00265	0.25	0.02	0.10
Total:			100.00		100.00

Figure 4.33. Table summary for EDS of elemental composition of CS coating and substrate. Values by percent weight are as expected for aluminum 6061.

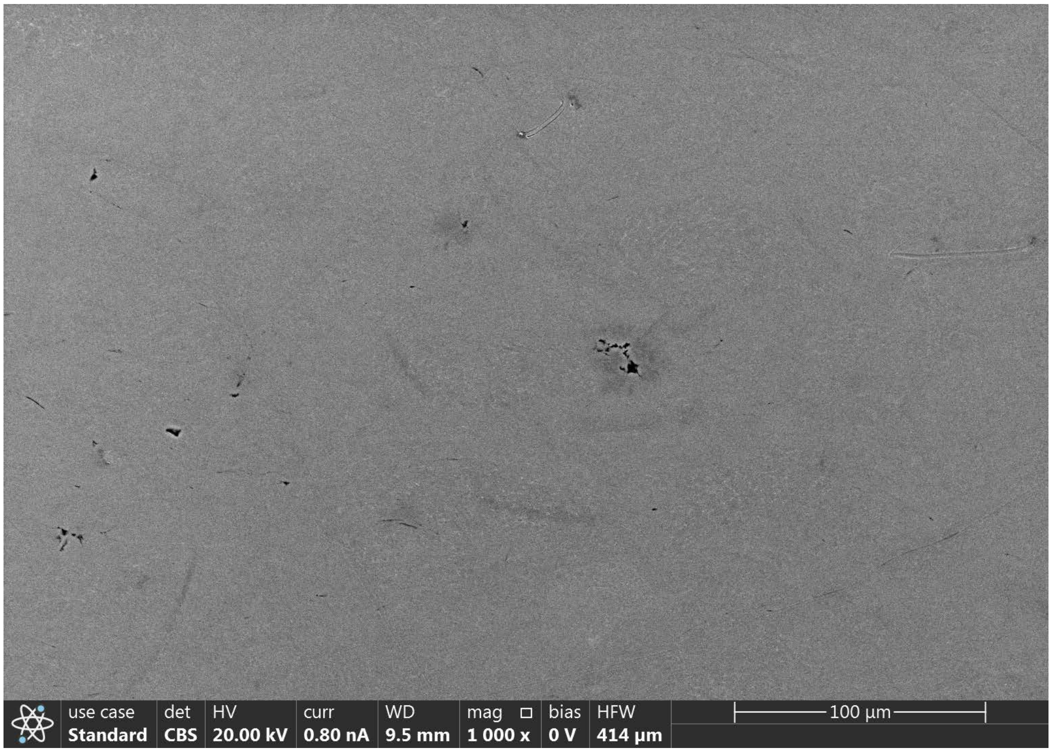

Figure 4.34. Bulk CS material in rib at midpoint showing increased porosity post-testing.

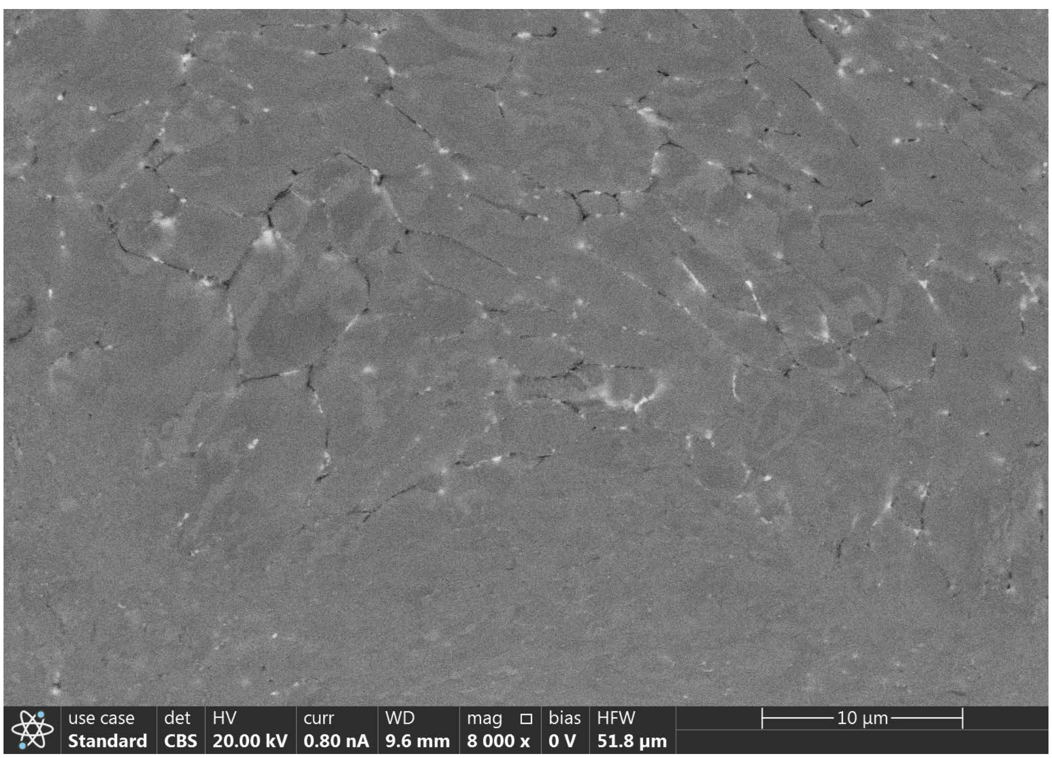

Figure 4.35. Particle level image showing interface between CS coating (top) and substrate (bottom).

Optical images of specimen V2282 were taken to supplement the SEM. Figures 4.36 and 4.37 are stitches images of the interface at the outer span and midpoint locations, respectively. The midpoint interface exhibits porosity along the length of the interface. Figures 4.38 and 4.39 are a better illustration of the differences in the coating. The outside span location has little porosity and the interface is not as easily identified due to the uniformity of the material. The midpoint's interface is apparent and porosity is present along the entire image. These optical images are in agreement with the SEM that not only is the bulk material more porous after undergoing load, but the interface as well where bonding was not strong enough to withstand the strains applied.

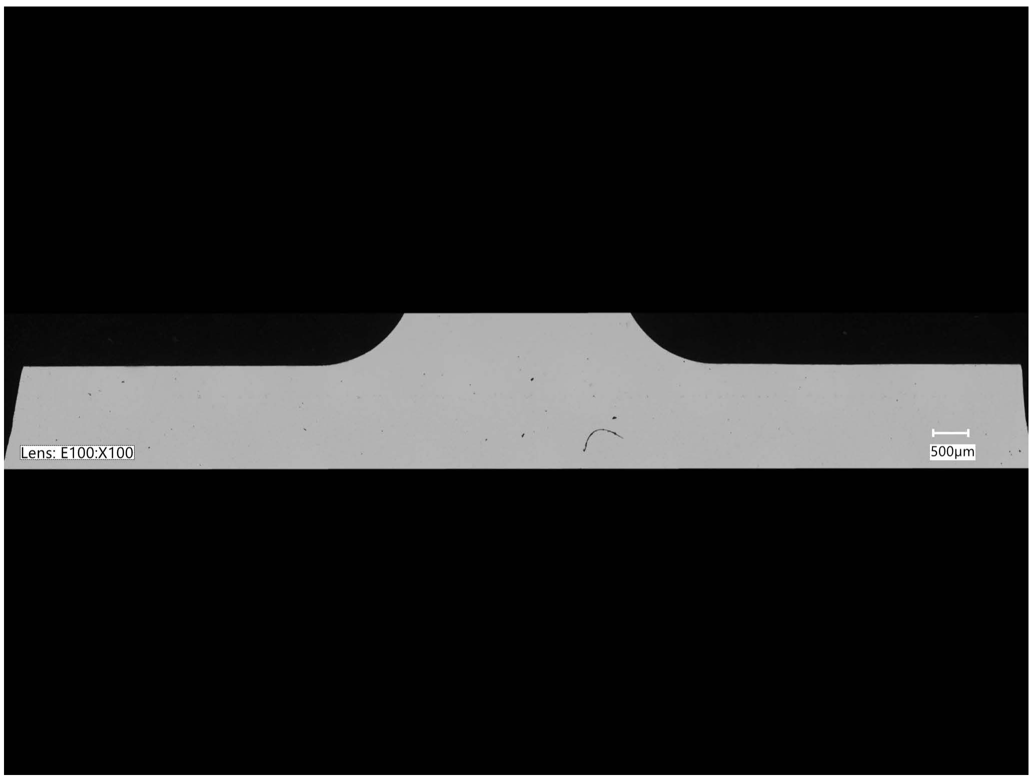

Figure 4.36. Cross-section image of the specimen at the outside span location.

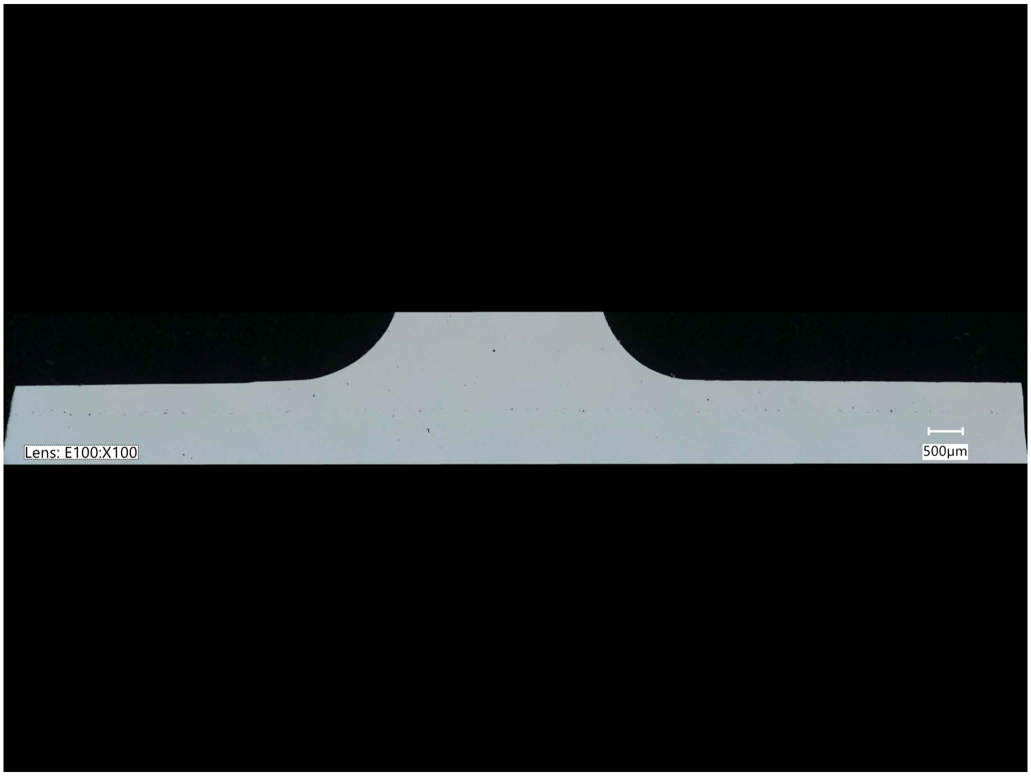

Figure 4.37. Cross-section image of the specimen at the midpoint.

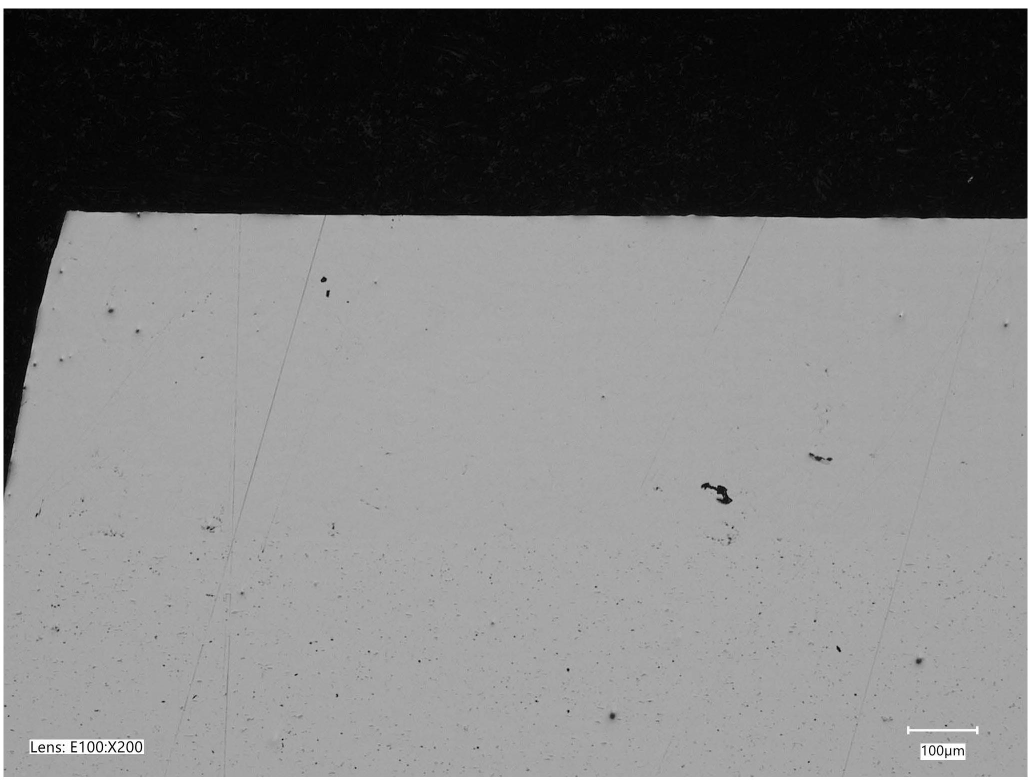

Figure 4.38. Magnified view of the interface at the outer span location.

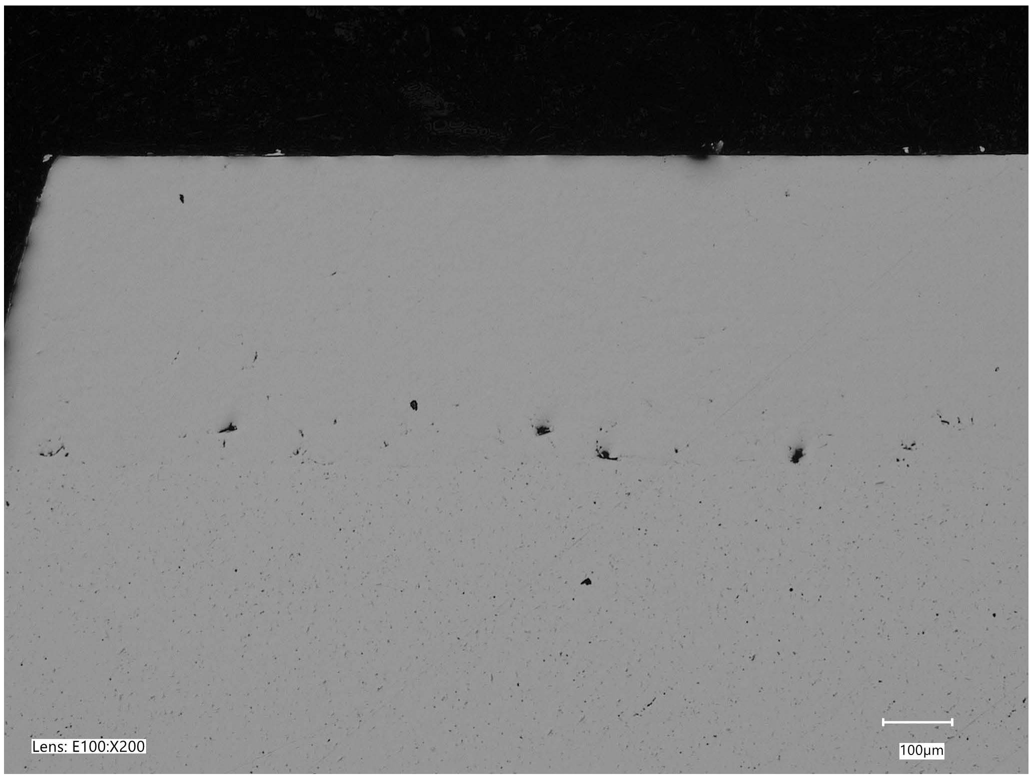

Figure 4.39. Magnified view of the midpoint location showing porosity along the interface that is not present in the outside span location.

4.4 Finite Element Modeling

4.4.1 Four-Point Bend Modeling Results

Plastic strain was extracted from the model results and compared to the strain data collected from the four-point bend tests on the MTS. On average, the strain data from the model was within 10% of the strain output recorded by the C4A gauges, post-test. The model's expected logarithmic strain was 0.85% for FE model while the strain gauges from the four-point tests averaged 0.8-1.0%. Figure 4.40 shows the contour plot of the strain in the longitudinal direction for the specimen. The red dot indicates the location of the strain values used to compare the model to empirical data. Given that displacement converges more quickly than stress, it was expected that the strain values would be in general agreement. The strain is also directly related to the stiffness of the material which is a more consistent parameter than the plastic behavior of a material. Strain outputs for the model were consistent regardless of the Johnson-Cook parameters used to predict post-yield behavior.

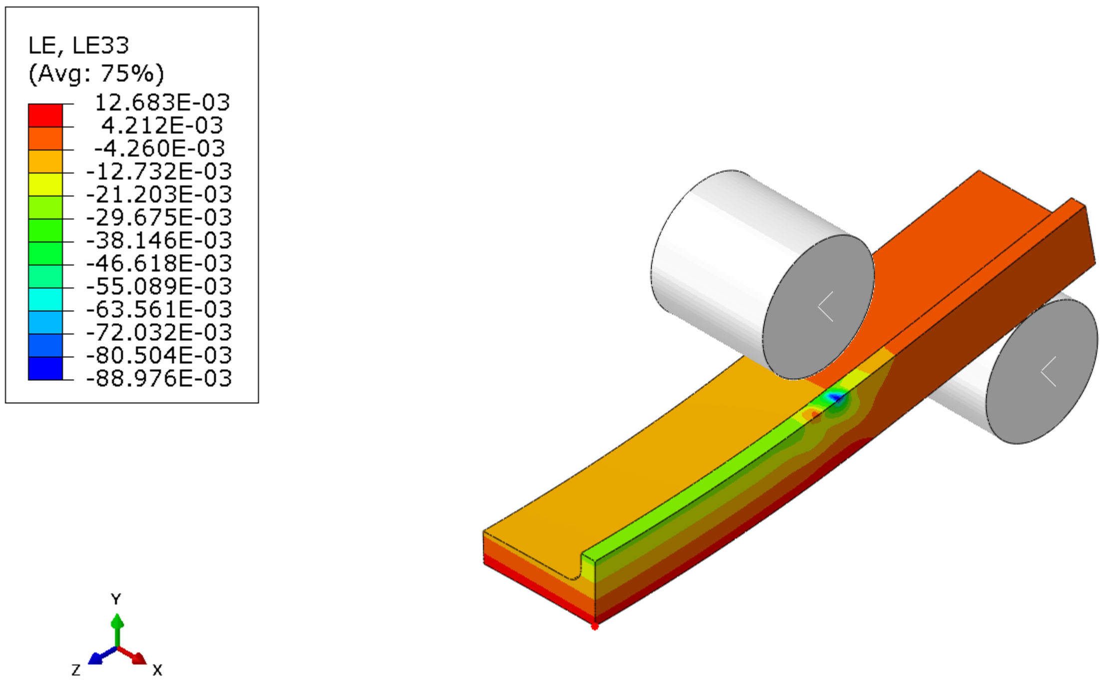

Figure 4.40. Logarithmic plastic strain of the specimen post-test. Roller displacement was returned to zero in the final analysis step to display the permanent deformation of the specimen.

4.4.2 Johnson-Cook Parameter Optimization

A finite element model was generated to provide comparison to the empirical data collected as well as provide a means of analyzing future cold sprayed specimens. The specimen was split into two sections to capture its multi-material composition, cold spray layer and wrought aluminum substrate. While the stiffness remained unchanged between the materials, the Johnson-Cook parameters were updated to account for the slightly weaker cold spray layer - 35 ksi yield instead of 38 ksi (see Appendix A.1 for substrate material certification). The goal of the model was to determine if the slight variation in performance could be predicted using the finite element method. Validation of the model could lead to future work with more complex geometries with the confidence that the material difference - powder and substrate - will be accurately captured for critical structural applications. Two material models were used, one for the wrought aluminum and one for the cold sprayed material, due to the slight difference in yield strength. The wrought aluminum had an expected yield strength of 38 ksi while the cold spray powder had a listed yield strength of 36 ksi. Johnson-Cook parameters for the wrought aluminum 6061-T6 material model for A, B, and n were 38 ksi, 20 ksi, and 0.1792, respectively [29].The temperature and strain rate dependent parameters were ignored in the model due to the low strain rate loading of the various test setups employed in this research. The J-C parameters from Manes et. al [29] were optimized for compression testing results and were expected to provide a first cut at modeling the four-point bend testing.

For the cold spray material model, the average J-C parameter A was determined to be 37.28$\pm$0.23 ksi (tensile test results in table 4.4) and serves as the 0.02% offset yield strength of the material. Parameters B and n were determined by processing the post yield data. True stress and true strain were plotted from the tensile test data. Equation 2.9 was transformed into equation 4.1 by subtracting yield strength (A) and taking the natural log of both sides. The y variable represents the natural log of the difference between the true stress and the yield stress. The x variable was the natural log of the plastic strain, determined by subtracting the strain at yield from all subsequent true strain values. This removes the elastic strain from the equation which is required for the calculation of stress when using the Johnson-Cook formula. Averaging the lines of best fit from Figures 4.41-4.43 resulted in average values of 50.17±2.64 ksi and 0.4855±0.012, for B and n respectively. These parameters, displayed in Table 4.6, were then used for the material model in the finite element model.

$$ln(\sigma_y - A) = n \cdot ln(\epsilon_{pl}) + ln(B) \tag{4.1}$$

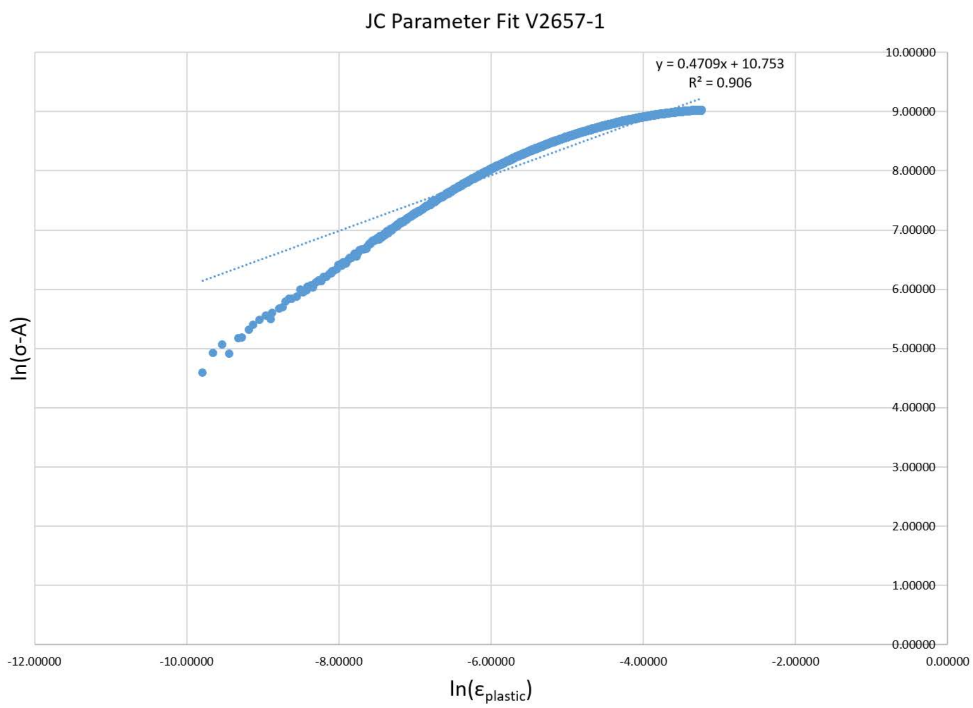

Figure 4.41. Relationship between ln($\sigma - A$) and ln($\epsilon_{plastic}$) for V2657-1, linear fit equation shown in upper right.

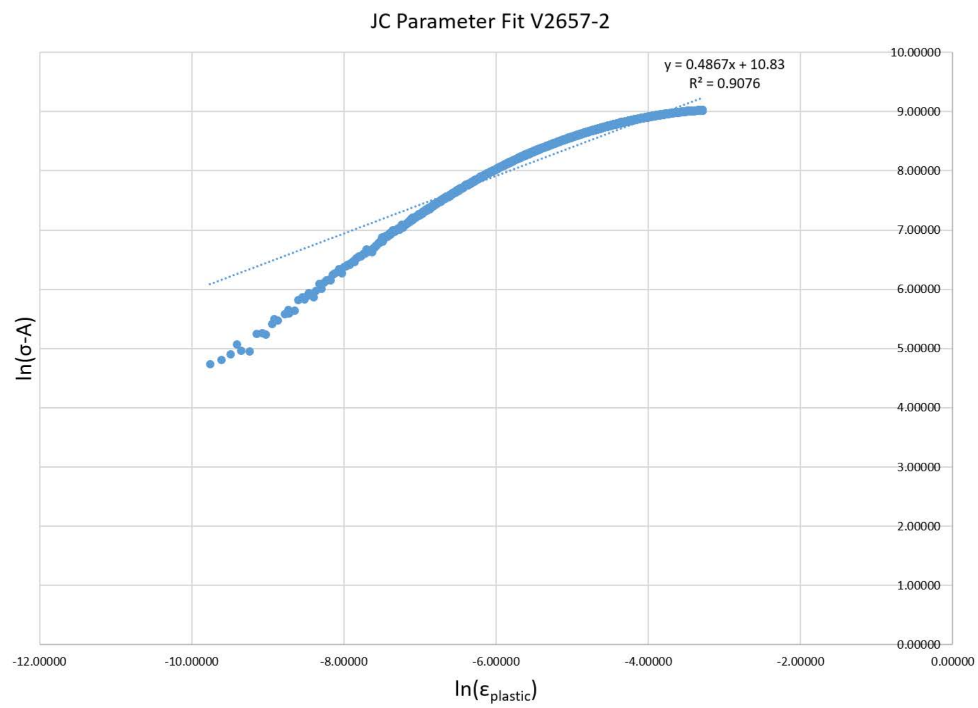

Figure 4.42. Relationship between $\ln(\sigma - A)$ and $\ln(\epsilon_{plastic})$ for V2657-2, linear fit equation shown in upper right.

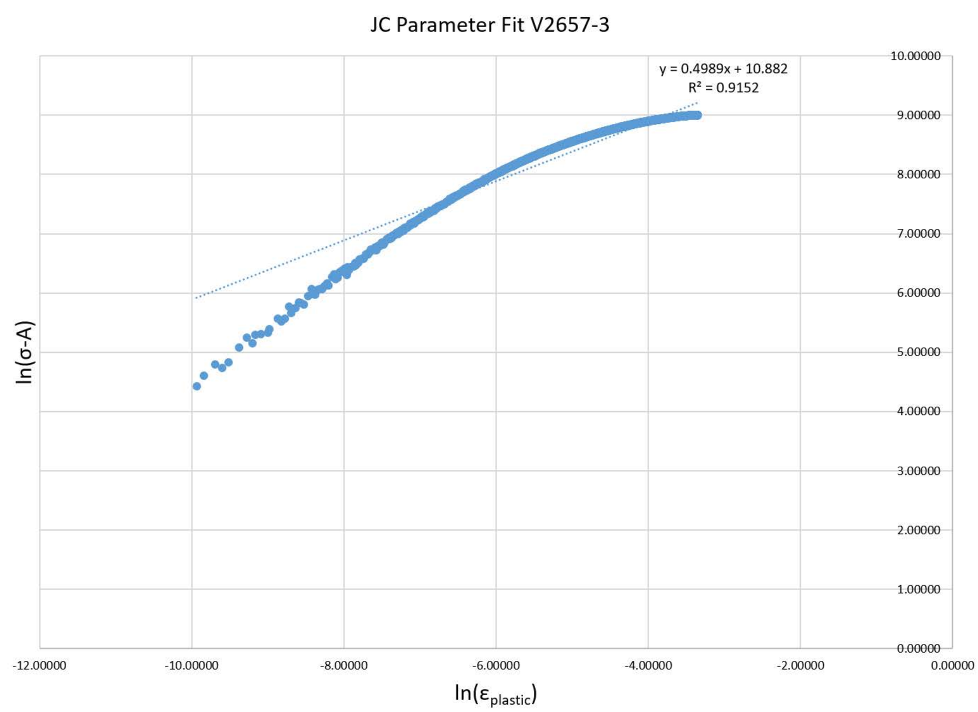

Figure 4.43. Relationship between $\ln(\sigma - A)$ and $\ln(\epsilon_{plastic})$ for V2657-3, linear fit equation shown in upper right.

Table 4.6. Averaged Johnson-Cook parameters from curve-fit equations.

A (psi)	**B (psi)**	**n**
37280±234	50165±2640	0.4855±0.012

Model results are shown in Figure 4.44. The results are in better agreement with the empirical results and average error is <5% until displacement exceeds 0.15 in. From this point onward, the model begins to deviate from the empirical results. A parameter sweep of n, the strain hardening exponent in the Johnson-Cook equation, was completed to determine if the value of n was impacting the force response at the higher deformations. Values of 0.1 to 0.5 in 0.1 increments were used for n in the cold spray material model to determine the sensitivity of the analysis to the strain hardening exponent. B was held constant since the model divergence appears to occur in the post-yield region where small changes to n can result in significant changes in the material's stress state. The error for a strain hardening exponent of 0.5 was 15% at the maximum displacement of 0.25 inches. An exponent of 0.2 - found in a research paper covering Al 6061 - resulted in an error of 30% with the model severely overestimating the strength of the specimen's post yield behavior [29]. At the same deformation, the finite element model predicted a maximum load of 725 lbs whereas empirical results averaged 600 lbf. For small amounts of plastic deformation, employment of the Johnson-Cook plasticity model works for determining the stress state of the specimen in bending; however, further exploration in future research efforts is needed to determine the cause of the overestimation of specimen strength and stiffness at higher levels of deformation.

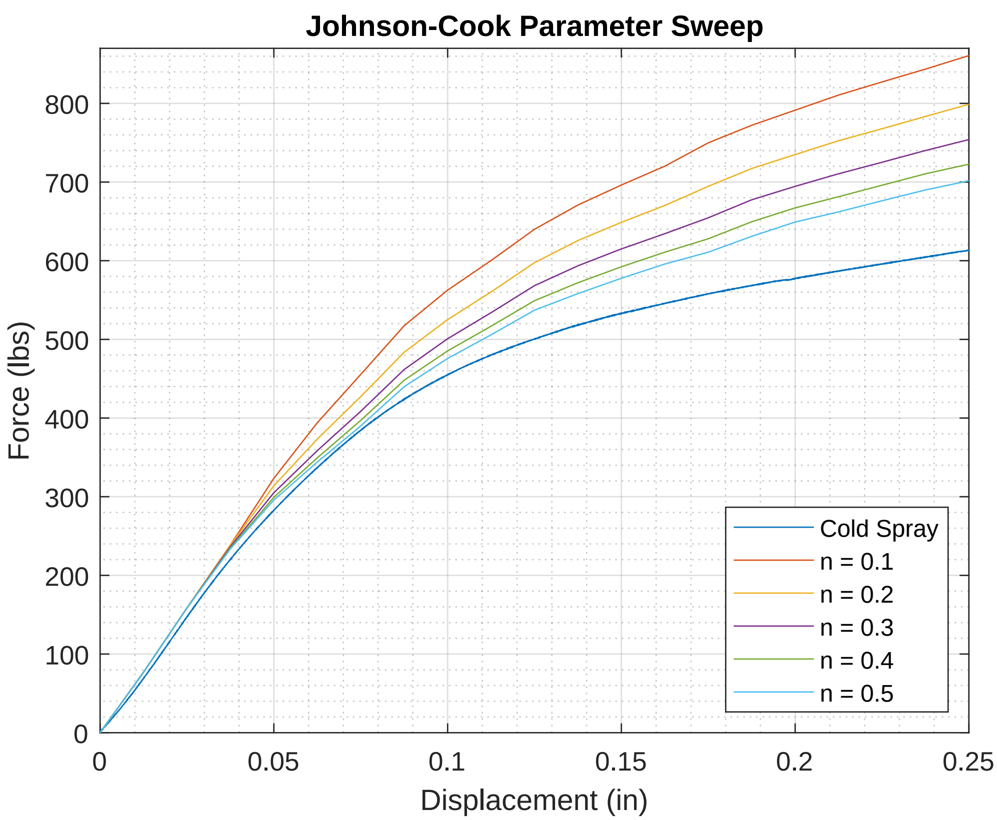

Figure 4.44. Modeling results for parametric study of Johnson-Cook parameter

Chapter 5
Conclusion

5.1 Summary

Four-point bending and tensile test results confirmed that the cold sprayed parts performed comparably to parts machined from stock material. Strain gauge data also shows a similar strain distribution in the maximum stress area of the two specimen types. The results of these tests confirm that additively manufacturing parts using cold spray would be a viable option. When used in the right applications, CS can save time and money. Coating thickness relative to substrate thickness is an area of interest to investigate further. A preliminary scaling of the part geometry showed that as the coating thickness increased, the residual stresses increased. When the coating thickness was doubled, the substrate began to warp by as much as .030” - measured at the mid-point of the specimen where maximum deflection was observed. Being cognizant of the coating thickness relative to the substrate thickness will undoubtedly limit the cases in which cold spray can be used as an additive manufacturing method. The effect of residual stresses could be mitigated by employing a more localized spraying approach which could be useful for threaded features and other bosses that would not affect the entire surface of the part. Conclusions listed categorically below.

Adhesion Testing:

- Glue failure occurred in the Solvay FM1000 epoxy adhesive for all four ASTM D4541 tests (>10 ksi CS coating bond strength)

Imaging:

- SEM revealed increase in porosity, or particle to particle separation, at the interface after testing
- Energy-dispersive spectroscopy (EDS) confirmed the elemental composition of the CS coating met the requirements for 6061 aluminum

CS Tensile Testing:

- Average yield strength: 37.3 ± 0.2 ksi
- Average ultimate strength: 43.8 ± 0.2 ksi
- Average elongation at break: 5.2 ± 0.3%

Four Point Bend Testing:

- Averaged data showed CS specimens were slightly stronger than the wrought aluminum as they required a 4.8% higher load (611 & 583 lbs, respectively) - at the maximum crosshead displacement of 0.250"
- CS specimens had a more consistent force-displacement response to bend testing than the wrought aluminum
- Strain data was observed to be the same between CS and wrought aluminum

Finite Element Analysis:

- Optimized values of A, B, and n using tensile data improved results of the FEA
- The Johnson-Cook plasticity model overestimates the stiffness of the specimen in the plastic region by 15% at the maximum crosshead displacement (0.250")
- Optimized values for A, B, and n were 37.3 ± 0.2 ksi, 50.2 ± 2.6 ksi, and 0.4855 ± 0.012, respectively.

5.2 Recommendations for Future Work

The results of this work are limited to the CS application of aluminum 6061 powder onto an aluminum 6061-T6 substrate. Further stress testing for different load applications is of interest as testing was limited to cold sprayed material in compression under a bending load. Future work could expand on different materials and their adhesion characteristics. A major area to be explored is the effect of the CS coating thickness applied to the substrate. The coating in these experiments was roughly .180" thick. In practice, coating thicknesses of a half inch or greater could be required when scaling up the size of the part being additively manufactured. The increased thickness of the coating affects the residual stresses in the part and the substrate's ability to resist these internal stresses would become essential to the manufacturing process. The implications of coating thickness results in a need for the substrate to maintain adequate rigidity during the cold spray process and limits the reduction of material to achieve a near-net shape. Depending on geometry of the desired part, the benefits of cold spray over a traditional near-net shape technique, such as forgings, could be diminished. The usefulness of utilizing cold spray as an additive manufacturing technique is highly dependent on part geometry. The scope of such an undertaking resulted in the variation of geometry being ignored for these experiments - future work should explore these variations and determine any shortcomings of cold sprayed parts in those configurations.

Future Areas of Research:

- Apply FEA model to different geometries
- Explore alternative plasticity models to accurately model CS coating
- Fatigue testing and the effect of cyclical loading on coating porosity & strength
- Explore location of interface as it relates to neutral axis. The interface for these specimens was near the neutral axis, limiting the stresses experienced during bending. Other geometries may not allow for the interface to be located near the neutral axis.

- Investigate porosity post-loading for various geometries
- Conduct testing for different materials
- Investigate and characterize effects of increasing coating thickness

Appendix A

McMaster-Carr Material Cert

Hydro

Hydro Extrusion USA, LLC
53 POTTSVILLE STREET
--
CRESSONA, PA
17929-0187

Certified Test Report

Sales Order Number	Line No.	Customer P/O	Cert Number	Page
1101661523	1	547327-1	HYDRO3263023	Page 2 of 2
			Cert Creation Date	**Cert Print Date**
			07-JUL-20	07-JUL-20

Alloy	Si PCT (%)		Fe PCT (%)		Cu PCT (%)		Mn PCT (%)		Mg PCT (%)		Cr PCT (%)		Zn PCT (%)	
	Min	Max	Min	Max	Min	Max	Min	Max	Min	Max	Min	Max	Min	Max
6061	0.40	0.80	---	0.70	0.15	0.40	---	0.15	0.80	1.20	0.04	0.35	---	0.25

Alloy	Ti PCT (%)		Others Each PCT (%)		Others Total PCT (%)	
	Min	Max	Min	Max	Min	Max
6061	---	0.15	---	0.05	---	0.15

Composition Results

Heat / Cast	Si	Fe	Cu	Mn	Mg	Cr	Zn	Ti	Others Each	Others Total
5052423	0.67	0.25	0.20	0.03	0.92	0.05	0.01	0.02	--	--

Mechanical Property - Test Limits

		Test Type	UTS - L		TYS - L		EL 4D-Long	
		UOM	KSI		KSI		PCT	
		# of Test	--		--		--	
Test Temper	Lot Number	# of Tests	MIN Value	MAX Value	MIN Value	MAX Value	MIN Value	MAX Value
T6511	23995371	1	41.7	41.7	38.3	38.3	14.5	14.5

Notes

Mercury is not a normal contaminant in aluminum alloys and we do not knowingly use it in the manufacture of our goods

Extruded in the USA

Extrusions produced to -T6511 temper also meet -T6 temper requirements

Figure A.1. Substrate material certification

Appendix B
ASTM E8 Specimen Drawing

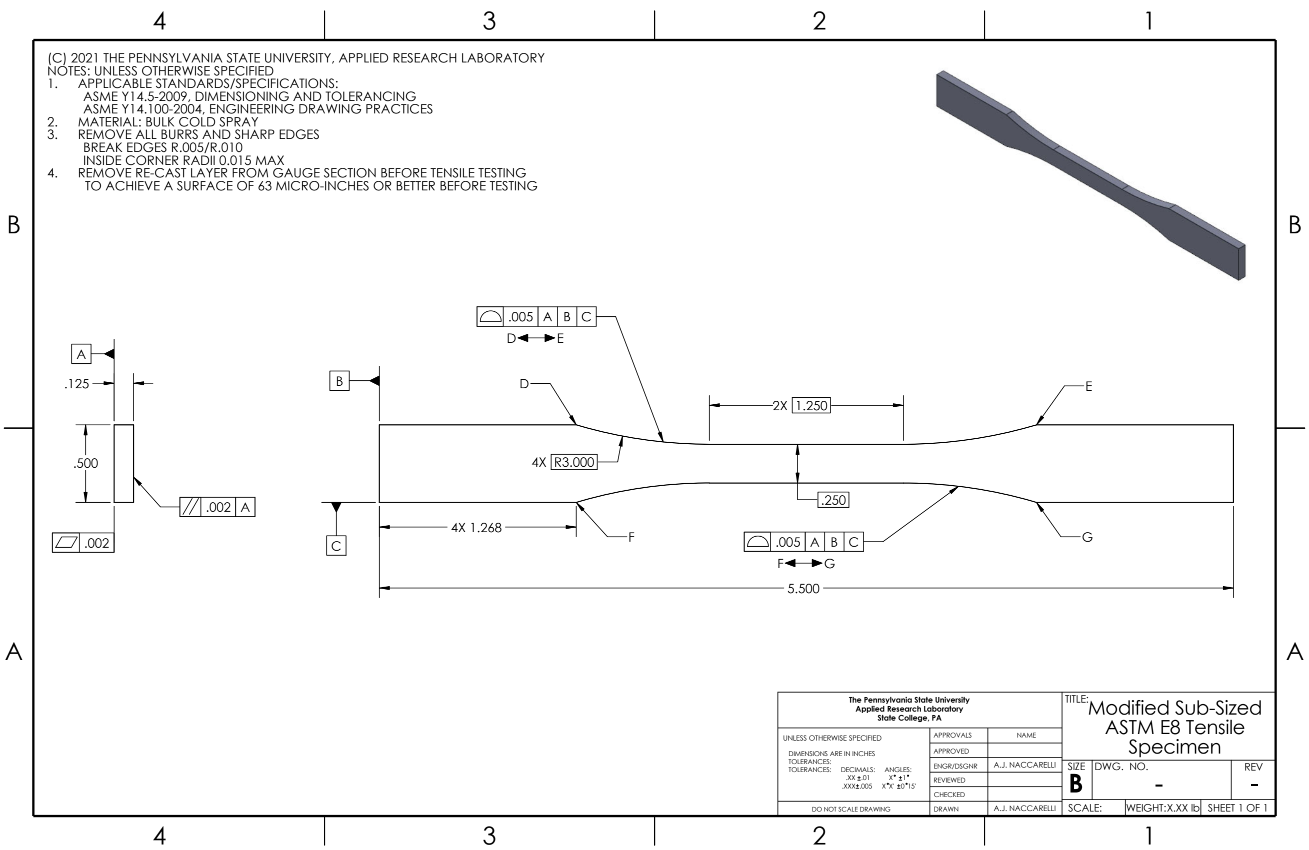

Figure B.1. Dogbone Drawing for Cold Spray Tensile Testing

Appendix C

Nontechnical Abstract

Cold spray is a material deposition process where a powder is deposited via high-pressure gas onto a stock piece of material, called the substrate. The buildup on the substrate results in a new, or repaired, part. Work needs to be done to validate the process and certify that cold sprayed parts perform on-par with parts that are machined from wrought aluminum. Near-net shape benefits and structural repair of high value parts that would otherwise need to be replaced in totality are a couple of the benefits. Parts were created with cold spray and test in four-point bending against parts machined from stock aluminum. Strain data was collected from the specimens to compare the deformation of the two specimen types. The results show that the strength of the cold sprayed specimens are adequate and in some cases more reliable than the machined from stock specimens. The strain data collected showed similar behavior between the two groups indicating that the overall stiffness of the cold sprayed parts was also comparable. The matching stiffness would be important for certain cases such as rib stiffeners in a cylindrical vessel where buckling is a concern. The ribs act as support to increase the stability of the part and allow substantial weight savings while maintaining the structural integrity of the part.

Bibliography

[1] Singh, H., T. Sidhu, S. Kalsi, and J. Karthikeyan (2013) "Development of cold spray from innovation to emerging future coating technology," *Journal of the Brazilian Society of Mechanical Sciences and Engineering*, **35**.

[2] Gavras, A. G., D. A. Lados, V. K. Champagne, and R. J. Warren (2018) "Effects of processing on microstructure evolution and fatigue crack growth mechanisms in cold-spray 6061 aluminum alloy," *International Journal of Fatigue*, **110**, pp. 49–62.

[3] Hodonou, C., M. Balazinski, M. Brochu, and C. Mascle (2019) "Material-design-process selection methodology for aircraft structural components: application to additive vs subtractive manufacturing processes," *The International Journal of Advanced Manufacturing Technology*, **103**, pp. 1509–1517.

[4] Assadi, H., F. Gärtner, T. Stoltenhoff, and H. Kreye (2003) "Bonding mechanism in cold gas spraying," *Acta Materialia*, **51**(15), pp. 4379–4394.
URL `https://www.sciencedirect.com/science/article/pii/S135964540300274X`

[5] Hassani-Gangaraj, M., D. Veysset, V. K. Champagne, K. A. Nelson, and C. A. Schuh (2019) "Response to Comment on "Adiabatic shear instability is not necessary for adhesion in cold spray"," *Scripta Materialia*, **162**, pp. 515–519.
URL `https://www.sciencedirect.com/science/article/pii/S1359646218307498`

[6] Stoltenhoff, T., H. Kreye, and H. Richter (2002) "An analysis of the cold spray process and its coatings," *Journal of Thermal spray technology*, **11**(4), pp. 542–550.

[7] Eden, T. "Process Description," in *The Cold Spray Materials Deposition Process: Fundamentals and Applications* (V. Champagne, ed.), chap. 2, Woodhead Publishing.

[8] Helfritch, D. and V. Champagne Jr (2008) "A Model Study of Powder Particle Size Effects in Cold Spray Deposition," , p. 6.

[9] Ozdemir, O. C., C. A. Widener, D. Helfritch, and F. Delfanian (2016) "Estimating the effect of helium and nitrogen mixing on deposition efficiency in cold spray," *Journal of Thermal Spray Technology*, **25**(4), pp. 660–671.

[10] Grujicic, M., C. Zhao, W. DeRosset, and D. Helfritch (2004) "Adiabatic shear instability based mechanism for particles/substrate bonding in the cold-gas dynamic-spray process," *Materials & Design*, **25**(8), pp. 681–688.
URL https://www.sciencedirect.com/science/article/pii/S026130690400069X

[11] Hassani-Gangaraj, M., D. Veysset, V. K. Champagne, K. A. Nelson, and C. A. Schuh (2018) "Adiabatic shear instability is not necessary for adhesion in cold spray," *Acta Materialia*, **158**, pp. 430–439.
URL https://www.sciencedirect.com/science/article/pii/S1359645418306050

[12] Nardi, A., D. Helfritch, O. C. Ozdemir, and V. K. Champagne (2021), "Process Control," .
URL https://doi.org/10.1007/978-3-030-70056-0_7

[13] Aldwell, B., E. Kelly, R. Wall, A. Amaldi, G. E. O'Donnell, and R. Lupoi (2017) "Machinability of Al 6061 deposited with cold spray additive manufacturing," *Journal of Thermal Spray Technology*, **26**(7), pp. 1573–1584.

[14] Villafuerte, J. (2014) "Considering cold spray for additive manufacturing," *Advanced Materials and Processes*, **50**, pp. 50–52.

[15] Yin, S., P. Cavaliere, B. Aldwell, R. Jenkins, H. Liao, W. Li, and R. Lupoi (2018) "Cold spray additive manufacturing and repair: Fundamentals and applications," *Additive manufacturing*, **21**, pp. 628–650.

[16] Moridi, A., S. M. H. Gangaraj, S. Vezzu, and M. Guagliano (2014) "Number of Passes and Thickness Effect on Mechanical Characteristics of Cold Spray Coating," *Procedia Engineering*, **74**, pp. 449–459, xVII International Colloquium on Mechanical Fatigue of Metals (ICMFM17).
URL https://www.sciencedirect.com/science/article/pii/S1877705814008662

[17] Gradl, P., D. Tinker, A. Park, O. Mireles, M. Garcia, R. Wilkerson, and C. Mckinney (2022) "Robust Metal Additive Manufacturing Process Selection and Development for Aerospace Components," *Journal of Materials Engineering and Performance*, **31**(8), pp. 6013–6044.
URL https://doi.org/10.1007/s11665-022-06850-0

[18] "Aluminum Alloy 6061 SPEE3D," .
URL https://www.spee3d.com/material/aluminium-alloy-6061-spd/

[19] Jahed, H. and R. Ghelichi (2015) *Residual Stresses and Fatigue Life Enhancement of Cold Spray*, Springer International Publishing, Cham, pp. 225–252.
URL https://doi.org/10.1007/978-3-319-16772-5_5

[20] Ghelichi, R., D. MacDonald, S. Bagherifard, H. Jahed, M. Guagliano, and B. Jodoin (2012) "Microstructure and fatigue behavior of cold spray coated Al5052," *Acta Materialia*, **60**(19), pp. 6555–6561.
URL https://www.sciencedirect.com/science/article/pii/S1359645412005496

[21] Wolfe, D. and T. Eden (2007) "14 - Cold spray particle deposition for improved wear resistance," in *The Cold Spray Materials Deposition Process* (V. K. Champagne, ed.), Woodhead Publishing Series in Metals and Surface Engineering, Woodhead Publishing, pp. 264–301.
URL https://www.sciencedirect.com/science/article/pii/B9781845691813500140

[22] Yamauchi, Y. and S. Miyaji (2014) "Interfacial state and characteristics of cold-sprayed copper coatings on aluminum substrate," *IOP Conference Series: Materials Science and Engineering*, **61**(1), p. 012023.
URL https://dx.doi.org/10.1088/1757-899X/61/1/012023

[23] Schmidt, T., F. Gärtner, H. Assadi, and H. Kreye (2006) "Development of a generalized parameter window for cold spray deposition," *Acta Materialia*, **54**(3), pp. 729–742.
URL https://www.sciencedirect.com/science/article/pii/S1359645405005975

[24] Schreiber, J., I. Smid, T. Eden, K. Koudela, D. Cote, and V. Champagne (2021) "Cold spray particle impact simulation using the Preston-Tonks-Wallace plasticity model," *Finite Elements in Analysis and Design*, **191**, p. 103557.
URL https://www.sciencedirect.com/science/article/pii/S0168874X2100041X

[25] Evans, W. C., X. Dan, A. Houshmand, S. Müftü, and T. Ando (2019) "Microstructural characterization of aluminum 6061 splats cold spray deposited on aluminum 6061-T6 substrate," *Metallurgical and Materials Transactions A*, **50**(8), pp. 3937–3948.

[26] Hall, A. C., D. Cook, R. Neiser, T. Roemer, and D. Hirschfeld (2006) "The effect of a simple annealing heat treatment on the mechanical properties of cold-sprayed aluminum," *Journal of Thermal Spray Technology*, **15**(2), pp. 233–238.

[27] Eden, T., A. Naccarelli, A. Birt, and J. Heelan "Cold Spray Economics," in *Advances in Cold Spray* (V. Champagne, D. Helfritch, and M. Hassani, eds.), 2nd ed., chap. 4, Woodhead Publishing.

[28] Widener, C., M. Carter, O. Ozdemir, R. Hrabe, B. Hoiland, T. Stamey, V. Champagne, and T. J. Eden (2016) "Application of high-pressure cold spray for an internal bore repair of a navy valve actuator," *Journal of Thermal Spray Technology*, **25**(1), pp. 193–201.

[29] Manes, A., L. Peroni, M. Scapin, and M. Giglio (2011) "Analysis of strain rate behavior of an Al 6061 T6 alloy," *Procedia Engineering*, **10**, pp. 3477–3482, 11th International Conference on the Mechanical Behavior of Materials (ICM11). URL https://www.sciencedirect.com/science/article/pii/S1877705811007612

[30] Tan, J. Q., M. Zhan, S. Liu, T. Huang, J. Guo, and H. Yang (2015) "A modified Johnson–Cook model for tensile flow behaviors of 7050-T7451 aluminum alloy at high strain rates," *Materials science & engineering. A, Structural materials : properties, microstructure and processing*, **631**, pp. 214–219.

[31] Farahani, H. K., M. Ketabchi, and S. Zangeneh (2017) "Determination of Johnson–Cook Plasticity Model Parameters for Inconel718," *Journal of materials engineering and performance*, **26**(11), pp. 5284–5293.

[32] Young, W. C. (1989) *Roark's Formulas for Stress and Strain*, McGraw-Hill.

[33] (2021) "ASTM B221 - Standard Specification for Aluminum and Aluminum-Alloy Extruded Bars, Rods, Wire, Profiles, and Tubes," ASTM International.

[34] (2016) "ASTM E8 - Standard Test Methods for Tension Testing of Metallic Materials," vol. 03.01, ASTM International.

[35] (2019) "ASTM E9 - Standard Test Methods of Compression Testing of Metallic Materials at Room Temperature," vol. 03.01, ASTM International.

[36] (2021) "ASTM E4 - Standard Practices for Force Calibration and Verification of Testing Machines," vol. 03.01, ASTM International.

[37] (2017) "ASTM E111 - Standard Test Methods of Standard Test Method for Young's Modulus, Tangent Modulus, and Chord Modulus," vol. 03.01, ASTM International.

[38] Batra, R. C. and M. H. Lear (2005) "Adiabatic shear banding in plane strain tensile deformations of 11 thermoelastoviscoplastic materials with finite thermal wave speed," *International Journal of Plasticity*, **21**(8), pp. 1521–1545.